Journal of Sound and Vibration 329 (2010) 1992–2014

Contents lists available at ScienceDirect

Journal of Sound and Vibration

journal homepage: www.elsevier.com/locate/jsvi

Experiment and analysis of a fuzzy-controlled piezoelectric seismic isolation system

Lyan-Ywan Lu [a,*], Chi-Chang Lin [b], Ging-Long Lin [b], Chen-Yu Lin [a]

[a] Department of Construction Engineering, National Kaohsiung First University of Science and Technology, 1 University Road, Yenchao, Kaohsiung 824, Taiwan
[b] Department of Civil Engineering, National Chung Hsing University, 250 Kuo-Kuang Road, Taichung 40227, Taiwan

ARTICLE INFO

Article history:
Received 8 July 2009
Received in revised form
13 December 2009
Accepted 14 December 2009
Handling Editor: A.V. Metrikine
Available online 8 January 2010

ABSTRACT

Because a conventional seismic isolation system is usually a long-period dynamic system, it may easily incur an excessive seismic response when subjected to near-fault earthquakes, which usually contain strong long-period wave components. In order to alleviate this near-fault isolation problem, this paper investigates the possible use of a fuzzy-controlled semi-active isolation system, called a piezoelectric seismic isolation system (PSIS), whose seismic response is attenuated by a variable friction damper driven by an embedded piezoelectric actuator. The studied PSIS adopts a fuzzy controller whose control logic is similar to that of the anti-lock braking systems (ABS) widely used in the automobile industry. This ABS-type fuzzy controller has the advantages of being simple and easily implemented, because it only requires the measurement of the PSIS sliding velocity. In order to investigate its feasibility and isolation effectiveness, in this work both theoretical and experimental studies were carried out on a prototype PSIS. It is observed that the experimental responses of the PSIS can be well predicted by the theoretical responses simulated by the mathematical model and numerical procedure. Furthermore, both theoretical and experimental results have demonstrated that in either a near-fault or a far-field earthquake, the PSIS with the ABS-type fuzzy controller is very effective in suppressing simultaneously the isolator displacement and the acceleration response of the isolated object.

1. Introduction

Seismic isolation technology has been successfully applied to protect seismic structures or equipment from usual earthquakes [1–3]. Nevertheless, recent studies have also discovered that a conventional isolation system, which is usually a long-period vibration system with a fixed fundamental frequency, may induce an excessive response in near-fault earthquakes [4]. According to many records of measured ground motions, it is observed that near-fault earthquakes usually have an intense long-period velocity pulse wave [5,6], whose pulse period usually ranges from 1.4 to 7 s. The long-period pulse wave component in a near-fault earthquake can result in harmful effects for an isolation system, such as an excessive isolator displacement and a decrease in isolation efficiency. These effects must be considered when a seismic isolation system is to be implemented in a near-fault region [4,7].

Since the characteristics of an earthquake are usually difficult to precisely predict, some researchers have proposed making seismic isolation systems more adaptive to excitations by adopting the technique of semi-active

* Corresponding author. Tel.: +886 7 6011000x2127; fax: +886 7 6011017.
E-mail address: lylu@ccms.nkfust.edu.tw (L.-Y. Lu).

0022-460X/$ - see front matter © 2009 Elsevier Ltd. All rights reserved.
doi:10.1016/j.jsv.2009.12.025

isolation, so that the aforementioned near-fault isolation problem can be alleviated. A semi-active isolation system, which is sometimes referred to as a smart isolation system, usually integrates a semi-active control device into an isolation system [8–10]. The semi-active device, whose dynamic behavior is adaptable to the excitation, can be in one of the several forms, such as: a variable fluid damper [11], a magneto-rheological (MR) damper [12–16], a resettable stiffness damper [17,18], a variable stiffness device [19–21] or a variable friction damper [22,23]. Unlike an active device, a semi-active device usually generates a passive resistant force that can be regulated by controlling some of its internal parameters [24]. Due to the above feature, as compared to passive and active isolation systems, a semi-active isolation system usually has the advantages of being more adaptable to the excitation, and having higher control stability and less control energy demand.

This paper primarily deals with a semi-active isolation system with a variable friction damper. Compared to other types of semi-active devices, friction-type damping devices generally have the advantage of being less vulnerable to the problems associated with fluid leakage, sediment of MR particles, aging materials and the influence of ambient temperature. A typical variable or semi-active friction damper usually consists of one or more friction interfaces and a controllable clamping mechanism that produces an adjustable normal (clamping) contact force on these interfaces [22,25,26]. By controlling the clamping force in real time, the slip force of a variable friction damper can be regulated in a way that enhances the performance of the controlled system. Furthermore, in order to determine the on-line control command for the clamping force, the implementation of a variable friction damper generally requires a control law. Numerous control methods have been developed in the literature for variable friction devices, and these can generally be classified as either discontinuous or continuous-force controls. A discontinuous-force control law is relatively simple and easily implemented, but it is usually accompanied by abrupt changes in the damper friction force that can exert a high-frequency response and increase the structural acceleration level [27,28]. In contrast, a continuous-force control law normally produces a smoother change of the friction force, resulting in a lower system acceleration response [29–32]. Nevertheless, a continuous-force control usually relies on an accurate system model and sensor measurement, and thus it is more sensitive to modeling errors or measurement noise.

To deal with uncertainties in the measurement or system modeling, control methods utilizing fuzzy set theory have been employed since the 1960s [33,34]. By incorporating human expertise into fuzzy IF–THEN rules, the primary advantage of a fuzzy controller is its inherent robustness and ability to handle nonlinearities and uncertainties in the structural behavior or external loadings [35]. Such fuzzy controllers have been applied successfully in various fields, including structural control [36–38]. Moreover, to effectively suppress earthquake induced motion, fuzzy controllers have also been successfully used in the control of building structures with MR dampers [15], semi-active hydraulic dampers [39], variable friction dampers [40], active mass dampers [41] and variable viscous dampers [42], among other applications.

Based on the above discussion, the purpose of this paper is to provide experimental and theoretical evidence for improving near-fault seismic isolation using a semi-active isolation system that utilizes variable friction and fuzzy logic control. To serve this purpose, a prototype semi-active isolation system, named a "Piezoelectric Seismic Isolation System (PSIS)", was fabricated and studied theoretically and experimentally in this work. The PSIS integrates a piezoelectric variable friction damper into a sliding isolation system. The friction force of the variable damper is regulated by an embedded actuator made of piezoelectric materials. Piezoelectric material is used for the actuation in this study because it has the advantages of being lightweight and having a low energy demand, swift response and easy implementation [43]. Furthermore, it must be emphasized that while there have been many studies on semi-active isolation systems with various semi-active devices, as mentioned above, very few of them involved experimental work, and these were only related to either an MR damper [44] or a variable stiffness device [19]. Thus, in the present literature, there is still insufficient test data or experimental evidence for semi-active isolation systems using variable friction dampers, even though the seismic energy dissipation of a building model using a variable friction damper has been tested by Chen and Chen [22].

Moreover, because the function of the piezoelectric friction damper in the PSIS is to dissipate kinetic energy and to mitigate the motion of the PSIS, this is similar to the function of a braking system in an automobile. For this reason, the proposed fuzzy controller for the PSIS is developed based on the concept of an antilock braking system (ABS), which is an efficient braking system widely used in the automobile industry [45]. In fact, some researchers have suggested the usage of fuzzy logic controllers in ABS systems [46,47]. Nevertheless, it must be remembered that the performance goals for a braking system and an isolation system are not completely identical. The former system aims to keep the maneuverability of the vehicle in the shortest braking distance [48,49], while the latter aims to reduce the structural acceleration with the smallest isolator displacement. Therefore, the conclusions obtained in the previous works on fuzzy ABS controllers for automobiles may not be directly applicable to seismic isolation systems.

The present paper is organized as follows. Firstly, the constituent elements and the configuration of the PSIS are introduced in Section 2, and then the ABS-type fuzzy controller is developed in Section 3. Section 4 introduces the mathematical model and the numerical procedure for the analysis of a structure isolated by the PSIS. Using this numerical procedure, Section 5 then evaluates the seismic performance of the PSIS with the proposed fuzzy controller, while Section 6 discusses the experimental results and isolation efficiency of the PSIS. Finally, the conclusions of the study are summarized in the last section.

2. Piezoelectric seismic isolation system (PSIS)

2.1. Configuration of the PSIS

Fig. 1 illustrates the schematic diagram of the PSIS presented in this work, which is mainly composed of a sliding isolation platform and a variable friction damper called a piezoelectric friction damper (PFD). The functions and the constituent elements of these two main components are explained below:

(1) *Sliding isolation platform*: The sliding platform functions as an isolation layer between the ground and the isolated object, so the transmitted ground acceleration can be reduced. As shown in Fig. 1, this sliding platform consists of the platform, sliding rails, sliding blocks and springs. The springs produce a linear resilient force that can prevent residual base displacement after an earthquake. Due to the existence of this resilient force, the PSIS has a constant isolation frequency. In addition, if the PFD damper is removed from the PSIS, the sliding platform alone becomes a conventional "passive" isolation system.

(2) *Piezoelectric friction damper* (*PFD*): The primary function of the PFD is to attenuate the seismic motion of the PSIS. Fig. 2 shows the front-view photograph of the PFD interior. As shown, a piezoelectric actuator is embedded in the PFD to generate a pair of controllable normal forces (clamping forces) $N(t)$ between the friction pads and the friction bar. When the PSIS is excited by an earthquake, the relative motion between the friction pads and the friction bar will

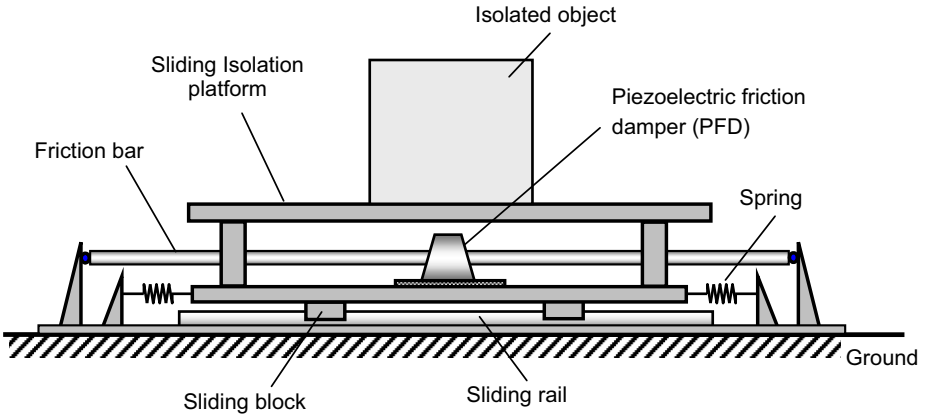

Fig. 1. Schematic diagram of the piezoelectric seismic isolation system (PSIS).

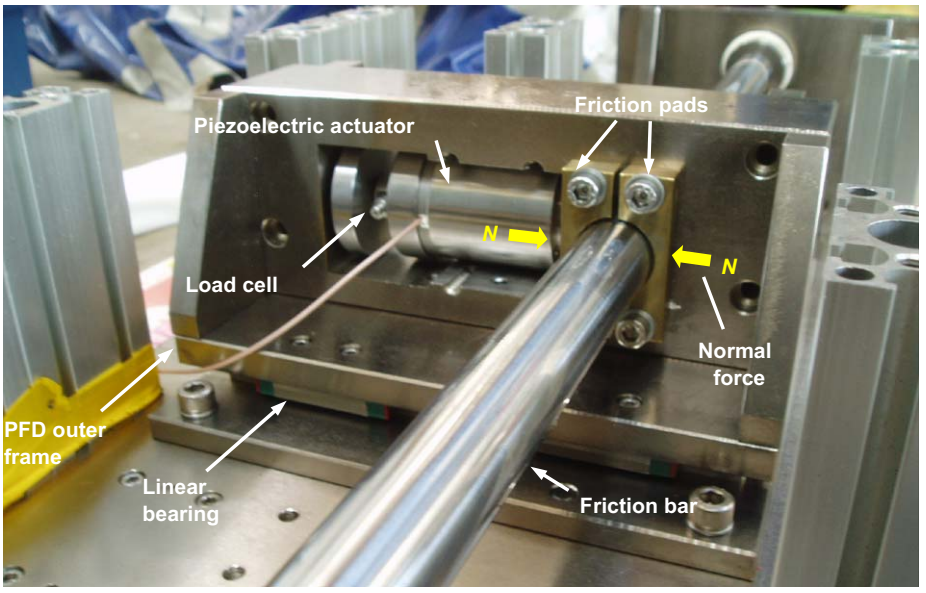

Fig. 2. Front-view photograph of the piezoelectric friction damper (PFD).

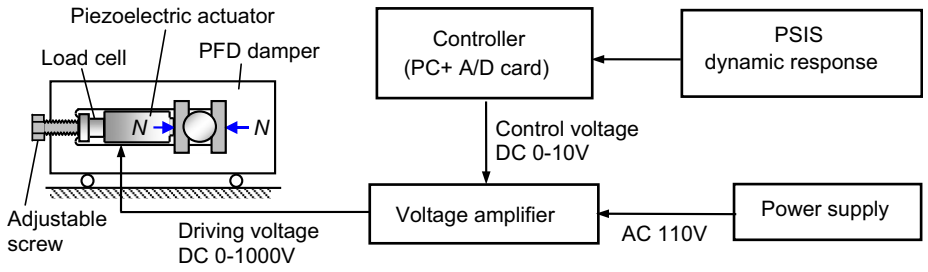

Fig. 3. Control block diagram of the PFD damper in PSIS.

generate a slip force that can be regulated by the piezoelectric actuator. Consequently, the seismic response of the whole PSIS is attenuated by the PFD through the actuator. Note that, as shown in Fig. 2, a set of low-friction linear sliding bearings is also installed below the outer frame of the PFD to make sure that the pair of normal forces are evenly produced. In addition, Fig. 2 also shows a load cell is placed against the piezoelectric actuator to measure the generated normal force $N(t)$. Finally, an adjustable screw (shown in Fig. 3) is bolted through the PFD outer frame and against the other side of the load cell, in order to generate a pre-compression force N_0 for the piezoelectric actuator.

2.2. Voltage control of the PFD damper

As mentioned previously, the friction force of the PFD is regulated by the piezoelectric actuator that is usually driven by a DC voltage. Fig. 3 shows the control block diagram of the piezoelectric actuator and the PFD. As shown in the figure, a voltage amplifier and a controller are usually required for the control of the PFD. The controller can be a simple digital controller that consists of a micro-computer (or a PC) and an analog/digital (A/D) converter card. The micro-computer will calculate the control command based on the sensor measurement of the current system response, whereas the card will convert the computed digital command into an analog signal, which is usually a DC voltage below 10 V. On the other hand, because the piezoelectric actuator may require a driving DC voltage up to 1000 V or higher, the control voltage provided by the controller's A/D converter is not sufficient to drive the piezoelectric actuator directly. For this reason, a voltage amplifier is needed to magnify the control voltage for the actuator. In this study, an amplifier with a gain of 100 V/V is used to amplify a 10 V control signal up to a driving voltage level of 1000 V. Nevertheless, the electric current required for the piezoelectric actuator is usually at a range of several mA, so the control energy demand for the PFD would be minimal.

The driving voltage is able to cause an elongation of the piezoelectric actuator in an unloaded condition. However, because the actuator is confined at its two ends by the outer frame of the PFD, a pair of the normal forces $N(t)$ are generated on the friction interfaces of the PFD by the friction pads (see Fig. 2). Moreover, since the elongation of the piezoelectric actuator is usually proportional to the driving voltage, the generated normal forces can be approximated by the following equation [23]:

$$N(t) = N_0 + C_z V(t) \tag{1}$$

where N_0 denotes the pre-compression force produced by turning the adjustable screw (see Fig. 3), $V(t)$ is the driving voltage of the piezoelectric actuator, C_z denotes a critical parameter called the piezoelectric coefficient of the actuator. As shown in Eq. (1), the increase of the force is proportional to the piezoelectric coefficient C_z. The physical meaning of C_z is the thrusting force of the actuator generated per driving voltage; therefore, C_z can be treated as a measure of the efficiency of the piezoelectric actuator. A larger C_z implies that a greater thrusting force can be generated by the actuator with a given voltage. Because the elongation of a piezoelectric actuator induced by the input voltage is usually in a range of only several tens of μm (10^{-6} m), the C_z value can be very sensitive to the confinement boundary condition of the actuator. As a result, the actual value of C_z for a specific application usually has to be identified experimentally.

Furthermore, according to Coulomb's friction law, the slip friction force $u_{d,\max}(t)$ (i.e., the maximum friction force) of the PFD should be dependent on the normal force $N(t)$. By using Eq. (1), this slip force can be written as

$$u_{d,\max}(t) = 2\overline{\mu}_d N(t) = \mu_d (N_0 + C_z V(t)) \tag{2}$$

where $\overline{\mu}_d$ denotes the material friction coefficient between the friction bar and friction pads (see Fig. 2), while $\mu_d = 2\overline{\mu}_d$ represents the total friction coefficient of the PFD. Note that $u_{d,\max}$ in Eq. (2) represents only the absolute value of the slip force. From Eqs. (1) and (2), it is evident that by altering the driving voltage $V(t)$, the normal force $N(t)$ and the slip force $u_{d,\max}(t)$ of the PFD can be controlled on-line and perform in the desired manner.

3. Fuzzy friction controllers for PSIS

As mentioned before, unlike the isolation of machine vibration, the aim of seismic isolation is to mitigate ground motion transmitted onto the isolated superstructure. Therefore, the performance indices that are used as a measure of seismic

isolation efficiency should be different from those used in machine isolation. In the field of earthquake engineering, the most commonly used isolation performance indices are related to the absolute structural acceleration and the relative base displacement (relative to the ground), because they are strongly related to design practice of isolation systems. More specifically, the absolute structural acceleration, multiplied by the structural mass, is equivalent to the total base shear of the isolated structure; while the base displacement is related to the design size of the seismic isolators. The isolated structure would fail, if its base shear in an earthquake exceeds the resistant capacity of its structural elements, while the isolation system would fail if its base displacement excited by an earthquake exceeds its designed size. In addition, the structural acceleration will also affect the structure's functionality, since a large acceleration level could damage the equipment inside the structure. Therefore, for a well-performed seismic isolation system, the structural acceleration and base displacement responses should be reduced and kept in an acceptable level. It is for this reason that the absolute structural acceleration (denoted by $\ddot{x}_{s,a}(t)$) and relative base displacement (denoted by $x_b(t)$) will be used to demonstrate the isolation performance of the PSIS in the latter sections of this study. Nevertheless, simultaneous reduction of the performance indices $x_b(t)$ and $\ddot{x}_{s,a}(t)$ of an isolation system is a very challenging task, especially when the system is subjected to a near-fault earthquake with long-period components. For a passive isolation system, the suppression of the base displacement $x_b(t)$ is usually achieved at the expense of increasing the structural acceleration $\ddot{x}_{s,a}(t)$ and sacrificing the isolation efficiency.

In order to simultaneously reduce $x_b(t)$ and $\ddot{x}_{s,a}(t)$ responses, in this study a fuzzy control law that is developed based on the concept of ABS systems for the control of the PFD in the PSIS will be proposed and explained in this section. The common goal of ABS systems is to brake the vehicle in the shortest distance, while avoiding a wheel lockup (i.e., when the rotation ceases) so that the maneuverability of the vehicle can be maintained. In order to have the shortest braking distance, an ABS system usually generates the largest possible brake force (clamping force) when the wheel is still rotating. However, in order to avoid a wheel lockup, the brake force (clamping force) is swiftly released when the wheel almost stops rotating. The above ABS control logic may also be applied to control the PFD of the studied PSIS. Because the basic principle of seismic isolation is to uncouple the motion of the isolated object from the ground excitation, at any instant the PFD damper should avoid applying a friction force that will "lock" the PSIS on the ground. In other words, the PFD should swiftly release its clamping force $N(t)$, whenever the velocity of the PSIS relative to the ground almost reduces to zero, so the PSIS can retain its seismic isolation function throughout an earthquake. On the other hand, in order to suppress the maximum displacement of the isolation system in an earthquake, the PFD should apply the largest possible clamping force $N(t)$ when the relative motion between the PSIS and the ground starts to increase. In brief, the PSIS control goal in this study is to reduce the isolator displacement, while avoiding the PSIS being locked on the ground, so that the efficiency of seismic isolation will not be reduced. In order to avoid the PSIS being locked on the ground due to the over-loaded clamping force $N(t)$, the proposed fuzzy controller chooses the relative sliding velocity of the isolation platform $\dot{x}_b(t)$, which is a direct indication of the PSIS state (stick or sliding), as the control feedback signal to determine the on-line command of the clamping force. However, it is emphasized that this control feedback signal $\dot{x}_b(t)$ should not be confused with the performance index responses $x_b(t)$ and $\ddot{x}_{s,a}(t)$ mentioned above.

Based on the above PSIS control goal, which mimics the control logic of an ABS braking system, a control method that utilizes a fuzzy inference system to determine the control voltage $V(t)$ for the PFD is proposed in this section. This fuzzy controller is labeled FC-15555 in Table 1. In addition, for the purpose of a comparative study to be conducted in a later section, two other controllers, labeled FC-13555 and FC-12345, are also listed in the table. The fuzzy rules of all three controllers are given in Table 1. As presented in the table, for all the controllers, the sliding velocity $\dot{x}_b(t)$ of the PSIS isolation platform is taken to be the only input variable (the only sensor measurement, or called control feedback), while the control voltage $V(t)$ of the piezoelectric actuator is the output variable. The sliding velocity $\dot{x}_b(t)$ (i.e., relative-to-the-ground velocity) of the platform can be treated as a measure of the occurrence of the relative motion between the PSIS and the ground. Moreover, as shown in Fig. 4(a), five membership functions are used for the input variable $\dot{x}_b(t)$ in all the fuzzy controllers. These five membership functions are labeled as ZE=zero, S=small, M=middle, L=large, and VL=very large. In addition, as shown in Fig. 4(b), the output variable $V(t)$ also uses five membership functions, labeled from 1 to 5, which represent the smallest to the largest subsets of the voltage levels, respectively. Fig. 4 also shows that the generalized bell-shaped functions are adopted for all membership functions of either the input or the output variables.

As presented in Table 1, according to the fuzzy rules of the FC-15555 controller, the maximum voltage ($V \in$ level 5) is applied by the piezoelectric actuator as soon as the PSIS starts to slide (i.e., $\dot{x}_b(t) \notin ZE$). Consequently, as shown in Eq. (2), the

Table 1
Comparison of the fuzzy rules for three fuzzy controllers.

Fuzzy controller name	Fuzzy rules	Controller input $\lvert\dot{x}_b\rvert$ (sliding velocity)				
		ZE	**S**	**M**	**L**	**VL**
FC-15555 (ABS-type)	Controller output V (driving voltage)	1	5	5	5	5
FC-13555		1	3	5	5	5
FC-12345		1	2	3	4	5

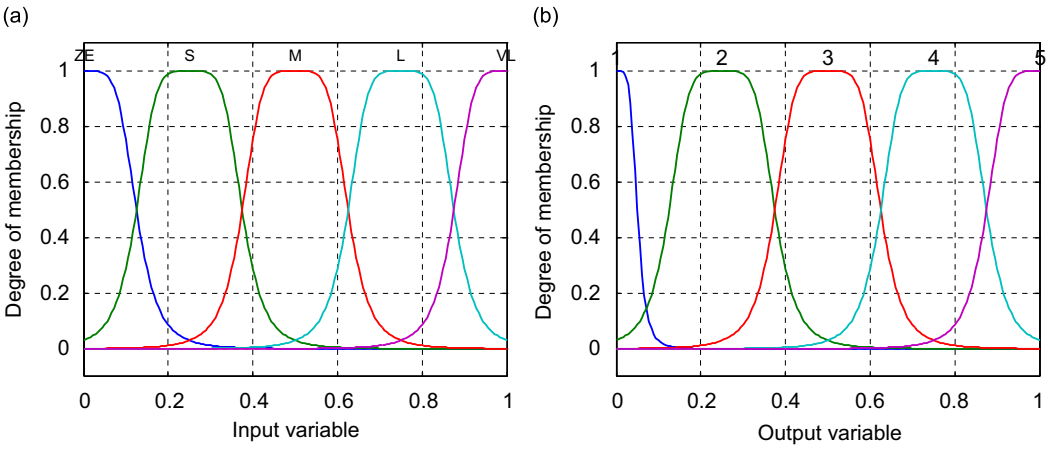

Fig. 4. Membership functions for the input and output variables: (a) input variable $\dot{x}_b(t)$, (b) output variable $V(t)$.

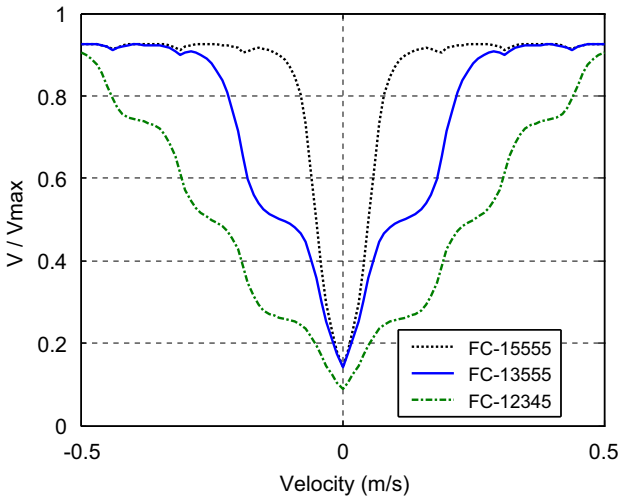

Fig. 5. Input and output relationships of the three fuzzy controllers.

PFD will reach its maximum slip force as $\dot{x}_b(t) \notin ZE$. This is very similar to the control logic of ABS systems, and thus the FC-15555 controller is called an ABS-type fuzzy controller in this study. On the other hand, the design concept for the fuzzy rules of the FC-13555 controller is basically similar to that for the FC-15555 controller, except that the driving voltage V is reduced to level 3 in the slow sliding velocity range (i.e., $|\dot{x}_b(t)| \in S$) for the purposes of comparison. In other words, the increase in the driving voltage in the FC-13555 controller is less sharp than that of the FC-15555. Finally, for the FC-12345 controller (see the last row of Table 1), the control voltage increases gradually and is roughly proportional to the sliding velocity of the isolation system. Therefore, the FC-12345 controller is similar to a proportional controller. Fig. 5 compares the input–output relations of the three fuzzy controllers. Notably, the driving voltage V of the actuator in the figure has been normalized with respect to its maximum value V_{max}. In Fig. 5, as expected, the FC-15555 rapidly increases the control voltage and reaches its maximum value once the PSIS starts to slide.

4. Numerical analysis method for the PSIS

4.1. Modeling of the PSIS

Fig. 6 shows the mathematic model of the PSIS isolated system adopted in this study. In the figure, the sliding isolation platform of the PSIS is modeled by a spring of the stiffness k_i and a friction element of the friction coefficient μ_i. The former is used to simulate the isolation stiffness due to the resilient mechanism, whereas the latter is used to model the friction effect of the sliding rail (see Fig. 1). On the other hand, in Fig. 6 the PFD is modeled by a variable friction element of a friction coefficient μ_d connected by a spring element of a stiffness k_d. The spring element k_d represents the axial stiffness of

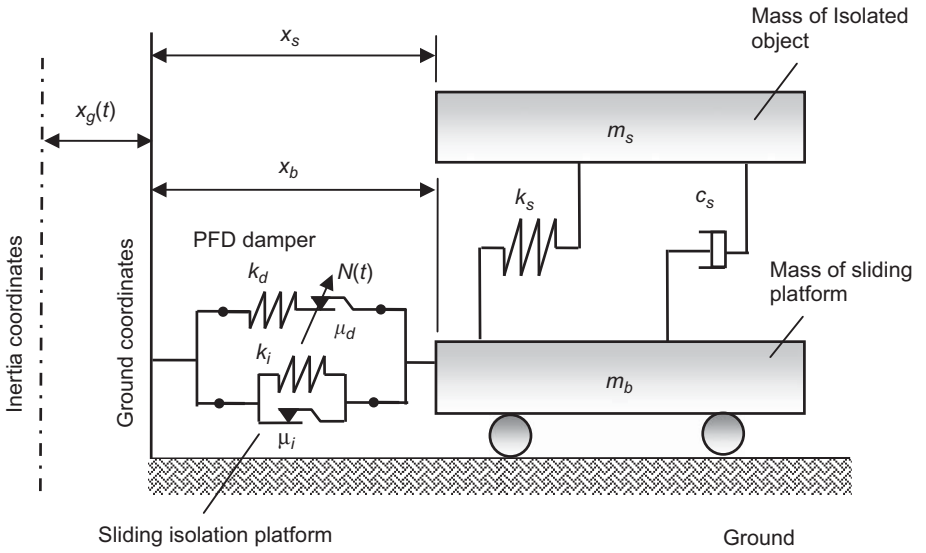

Fig. 6. Mathematical model of the PSIS isolated system.

the PFD damper. Moreover, the masses of the isolated object and sliding platform are denoted by m_s and m_b, respectively. For generality, the damping and stiffness of the isolated object itself are also considered in the model, and are denoted by the notations c_s and k_s in Fig. 6, respectively. The symbols x_s and x_b represent the relative-to-the-ground displacements of the isolated object and the isolation platform, respectively.

Based on the mathematical model shown in Fig. 6, the dynamic equation of the PSIS can be rewritten as

$$\mathbf{M}\ddot{\mathbf{x}}(t)+\mathbf{C}\dot{\mathbf{x}}(t)+\mathbf{K}\mathbf{x}(t)=\mathbf{D}_2(u_d(t)+u_i(t))+\mathbf{E}_1\ddot{x}_g(t) \tag{3}$$

where

$$\mathbf{x}(t)=\begin{Bmatrix} x_s(t) \\ x_b(t) \end{Bmatrix}, \quad \mathbf{D}_2=\begin{Bmatrix} 0 \\ -1 \end{Bmatrix}, \quad \mathbf{E}_1=\begin{Bmatrix} -m_s \\ -m_b \end{Bmatrix} \tag{4}$$

$$\mathbf{M}=\begin{bmatrix} m_s & 0 \\ 0 & m_b \end{bmatrix}, \quad \mathbf{C}=\begin{bmatrix} c_s & -c_s \\ -c_s & c_s \end{bmatrix}, \quad \mathbf{K}=\begin{bmatrix} k_s & -k_s \\ -k_s & k_s+k_i \end{bmatrix} \tag{5}$$

In Eq. (3), $\mathbf{x}(t)$ denotes the vector containing the system responses; $\ddot{x}_g(t)$ is the ground acceleration due to an earthquake; $\mathbf{D}_2$ and $\mathbf{E}_1$ denote the force placement vectors for the isolation system and the excitation, respectively. The matrices $\mathbf{M}$, $\mathbf{C}$ and $\mathbf{K}$ represent the mass, damping and stiffness matrices of the studied system. More importantly, in Eq. (3), $u_d(t)$ denotes the damper friction force provided by the PFD damper; $u_i(t)$ represents the friction force due to the sliding rail of the isolation platform.

Notably, as shown in Fig. 6 and Eq. (3), the primary system responses $x_s(t)$ and $x_b(t)$ are measured from the moving ground coordinates. As a result, the inertia force term $\mathbf{E}_1\ddot{x}_g(t)$ (also called seismic force) exerted by the ground acceleration, together with the PFD damper force u_d and sliding friction force u_i, can be moved to the right hand side of Eq. (3) and treated as external forces. Except the terms (u_i+u_d), Eq. (3) is actually a typical dynamic equation for seismic structures shown in many earthquake engineering textbooks [2]. It will be shown in Section 6 that the PSIS mathematical model depicted by Fig. 6 and described by Eq. (3) is successfully verified by the experimental data. Moreover, even though the force terms (u_i+u_d) in Eq. (3) have been treated as the external forces, the 2DOF system is a grounded system, because of the existence of the isolation stiffness k_i, which connects the PSIS and the ground and is kept inside the system stiffness matrix $\mathbf{K}$.

For the convenience of the numerical analysis, the dynamic equation of the PSIS can be rewritten in a state space form as below [50]

$$\dot{\mathbf{z}}(t)=\mathbf{A}\mathbf{z}(t)+\mathbf{B}(u_d(t)+u_i(t))+\mathbf{E}\ddot{x}_g(t) \tag{6}$$

where state vector $\mathbf{z}(t)$ contains the state variables of the PSIS and can be written as

$$\mathbf{z}(t)=[\dot{x}_s(t)\ \ \dot{x}_b(t)\ \ x_s(t)\ \ x_b(t)] \tag{7}$$

where $\dot{x}_s(t)$ and $\dot{x}_b(t)$ denote the relative-to-the-ground velocity of the isolated object and the isolation platform, respectively. Moreover, the system matrix $\mathbf{A}$ and the force placement matrices $\mathbf{B}$ and $\mathbf{E}$ can be written explicitly as

$$\mathbf{A}=\begin{bmatrix}-\mathbf{M}^{-1}\mathbf{C} & -\mathbf{M}^{-1}\mathbf{K}\\ \mathbf{I} & \mathbf{0}\end{bmatrix},\quad \mathbf{B}=\begin{bmatrix}\mathbf{M}^{-1}\mathbf{D}_2\\ \mathbf{0}\end{bmatrix},\quad \mathbf{E}=\begin{bmatrix}\mathbf{M}^{-1}\mathbf{E}_1\\ \mathbf{0}\end{bmatrix} \tag{8}$$

Note that the isolator stiffness k_i of the PSIS has been included in the matrix $\mathbf{K}$ (see Eq. (5)), so the system matrix $\mathbf{A}$ in Eq. (8) is a positive-definite matrix. Furthermore, it should be emphasized that, in view of Eq. (6) the damper force $u_d(t)$ is the only controllable force in the PSIS; therefore, the dynamic response of the whole system can be attenuated exclusively by altering $u_d(t)$ in real time. In addition, as discussed in Section 3 the fuzzy control command for $u_d(t)$ is solely determined by the relative velocity of the isolation platform $\dot{x}_b(t)$, therefore the output $y(t)$ of the above state-space system should be the relative velocity $\dot{x}_b(t)$, which can be written as

$$y(t)=\mathbf{D}_1\mathbf{z}(t)=\dot{x}_b(t) \tag{9}$$

where $\mathbf{D}_1=[0\ \ 1\ \ 0\ \ 0]$.

4.2. Discrete-time solution for the dynamic equation

As shown in Eq. (6), due to the existence of the friction forces $u_d(t)$ and $u_i(t)$, the PSIS subjected to a seismic load is a nonlinear system; therefore, a numerical method is generally required to analyze its dynamic response. The remainder of this section is devoted to explaining the numerical method adopted in this study to simulate the PSIS response. Before developing the method, it is assumed that the friction materials in the damper and isolators obey Coulomb's friction law and have equal static and dynamic friction coefficients. In order to obtain the discrete-time solution of Eq. (6), let us assume that the applied forces u_i, u_d and $\ddot{x}_g$ at the right-hand side of Eq. (6) are constant within each sampling period Δt (time step of analysis), so the time integration of Eq. (6) over the sampling period would lead to the following discrete-time state equation.

$$\mathbf{z}[k+1]=\mathbf{A}_d\mathbf{z}[k]+\mathbf{B}_d(u_i[k]+u_d[k])+\mathbf{E}_d\ddot{x}_g[k] \tag{10}$$

where

$$\mathbf{A}_d=e^{\mathbf{A}\Delta t}$$

$$\mathbf{B}_d=\mathbf{A}^{-1}(\mathbf{A}_d-\mathbf{I})\mathbf{B}$$

$$\mathbf{E}_d=\mathbf{A}^{-1}(\mathbf{A}_d-\mathbf{I})\mathbf{E} \tag{11}$$

In Eq. (10), a quantity with $[k]$ indicates that the quantity is evaluated at the k-th time step of analysis. The detailed derivation of the above discrete-time state equation has been given in [50], interested readers may refer to it. Notably, Eq. (10) uses an explicit integration scheme for the system of ODEs. Such numerical schemes usually have limited stability regions. To this end, a smaller size of the time step Δt is usually required to ensure the accuracy and stability of the numerical result. $\mathbf{A}_d$, $\mathbf{B}_d$, and $\mathbf{E}_d$ in Eq. (11) are all constant matrices. Eq. (10) is an incremental equation in time domain, because it states that the system response $\mathbf{z}[k+1]$ of the next time step (i.e., the $(k+1)$th time step) can be computed based on the current step (the kth step) information, including the state $\mathbf{z}[k]$, excitation $\ddot{x}_g[k]$, friction forces $u_i[k]$ and $u_d[k]$. Note that $\mathbf{z}[k]$ has already been determined at the previous time step by using Eq. (10) with the index k replaced by $(k-1)$. However, the terms $u_i[k]$ and $u_d[k]$ in Eq. (10) are both unknown nonlinear friction forces at the beginning of the kth step computation. The computations of $u_i[k]$ and $u_d[k]$ will be explained in detail in Sections 4.3 and 4.4, respectively. The computational method is derived based on the shear-balance method [51,52], which is a very efficient numerical method to deal with dynamic systems with friction elements or dampers.

4.3. Determination of damper friction force $\boldsymbol{u_d[k]}$

Since the PFD damper is installed between the base of the PSIS and the ground (see Fig. 6), at any time instant the PSIS base displacement $x_b[k]$ is equal to the damper elongation that consists of two components, as illustrated in Fig. 7, i.e.,

$$x_b[k]=d_e[k]+d_f[k] \tag{12}$$

where $d_e[k]$ and $d_f[k]$ denote the elastic deformation and the slip displacement of the PFD damper, respectively. Moreover, since $d_e[k]$ is the elastic deformation due to the damper stiffness k_d, its value must depend on the damper axial force $u_d[k]$, i.e.,

$$u_d[k]=k_d d_e[k] \tag{13}$$

Next, using the relation $x_b[k]=\mathbf{D}\mathbf{z}[k]$ and Eq. (12) into Eq. (13), one has

$$u_d[k]=k_d(\mathbf{D}\mathbf{z}[k]-d_f[k]) \tag{14}$$

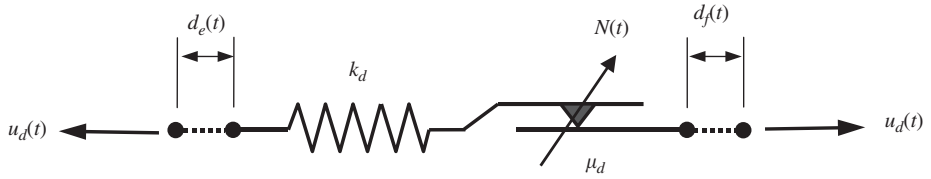

Fig. 7. Elongation of the PFD damper.

where $\mathbf{D}=[0\ 0\ 0\ 1]$ is a row vector. As shown in Eq. (14), the damper friction force $u_d[k]$ is a function of the state vector $\mathbf{z}[k]$ and the unknown slip displacement $d_f[k]$, which is an independent variable that is not included in the state vector $\mathbf{z}[k]$. Since $d_f[k]$ is unknown at the beginning of the k-th step computation, so is $u_d[k]$. To overcome this problem, the shear-balance method [52], which is able to compute $u_d[k]$ without the calculation of $d_f[k]$, is explained below.

It is known that the motion of a friction damper has two exclusive states, i.e., stick and slip, and at any given time instant the damper can only be in one of these states. Now, if we assume that in the time interval from the $(k-1)$th to the kth time steps the damper is in its stick state, then the following damper kinematic condition must be satisfied

$$d_f[k] = d_f[k-1] \tag{15}$$

Next, by using Eq. (15) in Eq. (14), and then subtracting $u_d[k-1]$ from $u_d[k]$ of Eq. (14), one has

$$\tilde{u}_d[k] = k_d\mathbf{D}(\mathbf{z}[k]-\mathbf{z}[k-1]) + u_d[k-1] \tag{16}$$

Inspecting Eq. (16), one notes that $\tilde{u}_d[k]$ can be readily computed, since all the values of $\mathbf{z}[k]$, $\mathbf{z}[k-1]$, $u_d[k-1]$ are determined based on the previous-step response, i.e., the $(k-1)$th step response. Note that in the left-hand side of Eq. (16), $u_d[k]$ is replaced by a new symbol, $\tilde{u}_d[k]$, to signify that the damper force is obtained under the stick-state assumption. The physical meaning of $\tilde{u}_d[k]$ actually represents the friction force required at the kth time step, in order to keep the damper in its stick state. At a certain time step, if $\tilde{u}_d[k]$ is greater than the adjustable slip force $u_{d,\max}[k]$ determined by Eq. (2), the damper will not be in its stick state at that step, but rather in its slip state. Therefore, although $\tilde{u}_d[k]$ may or may not be the actual friction force, it plays a very important role in deciding the motion status (stick or slip) and the actual friction force of the PFD damper. The above statement can be expressed by the following equations.

(a) If $|\tilde{u}_d[k]| < u_{d,\max}[k]$, the PFD is in its stick state and the damper friction force is

$$u_d[k] = \tilde{u}_d[k] \tag{17}$$

(b) If $|\tilde{u}_d[k]| \geq u_{d,\max}[k]$, the PFD is in its slip state and the damper friction force is

$$u_d[k] = u_{d,\max}[k]\mathrm{sgn}(\tilde{u}_d[k]) \tag{18}$$

where the damper slip force $u_{d,\max}[k]$ is related to the driving voltage $V[k]$ through Eq. (2), i.e.,

$$u_{d,\max}[k] = \mu_d(N_0 + C_z V[k]) \tag{19}$$

It must be remembered that the voltage $V[k]$ in Eq. (19) is determined by one of the fuzzy controllers introduced in the last section. In Eq. (18), the function $\mathrm{sgn}(a)$ means taking the sign of the variable a. As mentioned previously, because $\tilde{u}_d[k]$ physically represents the friction force required at the kth time step to keep the damper in its stick state, $\mathrm{sgn}(\tilde{u}_d[k])$ indicates the tendency of the resistant force of the PFD, and thus it is also used to represent the direction of the damper slip force in Eq. (18). For simplicity, Eqs. (17) and (18) can also be merged into the following equation, which is applicable to both the slip and stick states of the damper.

$$u_d[k] = \min(|\tilde{u}_d[k]|, u_{d,\max}[k])\mathrm{sgn}(\tilde{u}_d[k]) \tag{20}$$

where the function $\min(a, b)$ means taking the minimum value among a and b.

4.4. Determination of isolator friction force $u_i[k]$

After the controllable force $u_d[k]$ is determined by Eq. (20), the friction force $u_i[k]$ due to the sliding rail of the isolation platform can now be calculated. To do so, let us first assume that from the k-th time step to the $(k+1)$th step, the sliding platform is in its stick (non-sliding) state, so the relative velocity $\dot{x}_b[k+1]$ of the isolation platform must be equal to zero, i.e.,

$$\dot{x}_b[k+1] = \mathbf{D}_1\mathbf{z}[k+1] = 0 \tag{21}$$

where $\mathbf{D}_1 = [0\ 1\ 0\ 0]$. Next, substituting $\mathbf{z}[k+1]$ from Eq. (10) into Eq. (21), then solving the equation for the friction force $u_i[k]$, one may obtain

$$\tilde{u}_i[k] = \mathbf{G}_z\mathbf{z}[k] + G_u u_d[k] + G_w\ddot{x}_g[k] \tag{22}$$

where

$$\mathbf{G}_z = -(\mathbf{D}_1\mathbf{B}_d)^{-1}(\mathbf{D}_1\mathbf{A}_d)$$

$$G_u = -1$$

$$G_w = -(\mathbf{D}_1\mathbf{B}_d)^{-1}(\mathbf{D}_1\mathbf{E}_d) \tag{23}$$

Note that $u_i[k]$ in Eq. (22) is replaced by the symbol $\tilde{u}_i[k]$ to signify that the obtained friction force is under the stick-state assumption. Similar to $\tilde{u}_d[k]$, the physical meaning of $\tilde{u}_i[k]$ is the friction force required to keep the sliding platform in its stick state, and it will be the actual friction force if the isolation platform is really in its stick state. On the other hand, if the isolation platform is actually in its sliding state, the friction force must be equal to the sliding force, which can be written as

$$u_i[k] = u_{i,\max}\,\mathrm{sgn}(\tilde{u}_i[k]) \tag{24}$$

where $u_{i,\max}$ denotes the absolute sliding force (the maximum friction force) of the isolation platform, which is related to the total weight of the system, i.e.,

$$u_{i,\max} = \mu_i(m_s + m_b)g \tag{25}$$

where μ_i represents the friction coefficient of the sliding isolation platform (see Fig. 6). Furthermore, at any time instant, the isolation platform should be physically either in its stick state or sliding state. No matter in which state, the absolute

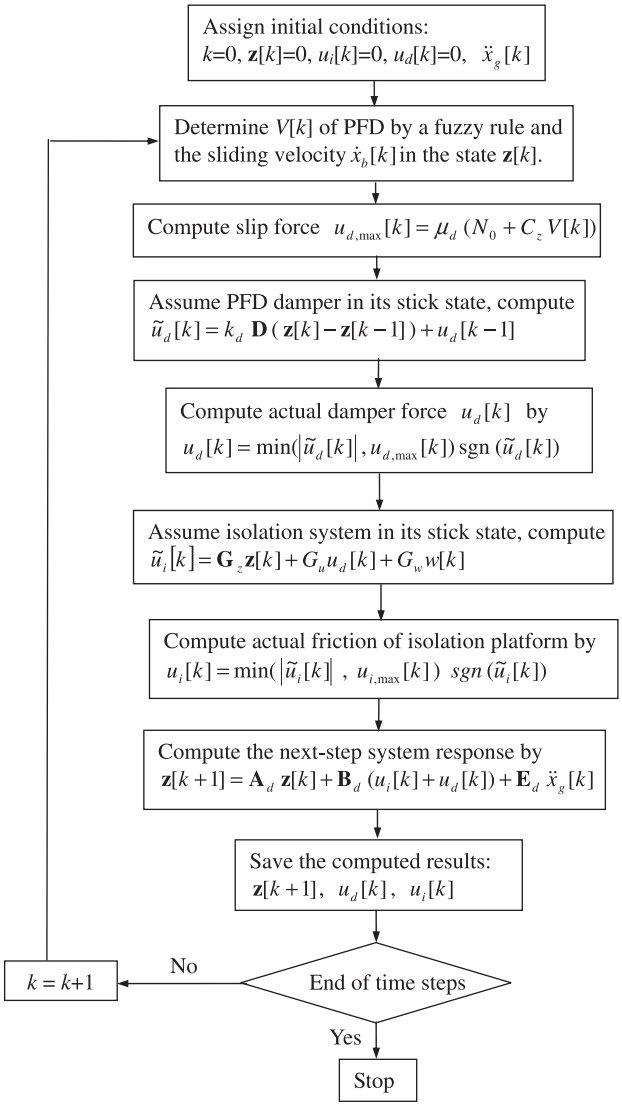

Fig. 8. Computational flowchart for the numerical analysis procedure.

value of the actual $u_i[k]$ cannot be greater than $u_{i,\max}$; therefore, the actual friction force can be expressed as

$$u_i[k] = \min(|\tilde{u}_i[k]|, u_{i,\max}[k])\mathrm{sgn}(\tilde{u}_i[k]) \tag{26}$$

Note that, similar to Eq. (20), Eq. (26) is applicable to both the stick and sliding states of the isolation platform.

After $u_d[k]$ and $u_i[k]$ are determined by Eqs. (20) and (26), respectively, they can be substituted back into Eq. (10) to complete the computation of the $(k+1)$th step system response $\mathbf{z}[k+1]$. The above numerical procedure of using Eq. (10) is executed step by step until the complete time history of the system response is obtained. Fig. 8 depicts the computational flowchart of the numerical procedure discussed in this section. As shown in the figure, the computational process is fairly straightforward, and easily implemented numerically.

5. Numerical study on the prototype PSIS

As discussed in Section 3, three fuzzy friction controllers have been designed for the control of the PSIS, as presented in Table 1, of which FC-15555 represents the ABS-type controller. By using the numerical simulation method explained in Section 4, this section will investigate theoretically the isolation performance of these controllers when the PSIS is subjected to different types of earthquake. In the numerical simulation, the values of the system parameters were taken from a prototype PSIS, which was tested in the shaking table test discussed in the next section. This section will first explain the properties of the prototype PSIS and the characteristics of the ground motions used in the study, and then the results from the simulation will be discussed.

5.1. Prototype PSIS

Fig. 9 shows a photograph of the prototype PSIS that was used in the numerical and experimental studies of this work. As shown in the photograph, in order to focus on the dynamic behavior of the PSIS itself, a set of rigid mass blocks directly bolted on the isolation platform was used to simulate the mass of the isolated superstructure (i.e., the isolated object). Table 2 lists the properties and the parameter values of this prototype PSIS. These values were obtained from identification or calibration tests, and will be used in the numerical simulation throughout this study. In Table 2, it is presented that the PSIS has a typical isolation frequency of about 0.41 Hz. Since the isolated structure is modeled as a rigid body, the identified isolation frequency ω_i=0.41 Hz is equivalent to the first natural frequency of the whole PSIS isolated system (sliding platform and isolated structure combined system). This isolation frequency falls into the commonly used frequency range for seismic isolation design (see Ref. [2]).

Moreover, the parameters inside matrices **K** and **C** are also listed in Table 2. As shown in Eq. (5) and Table 2, there are two independent parameters k_i and k_s in matrix **K**, while there is only one parameter c_s in matrix **C**. The isolation stiffness k_i was computed based on the identified isolation frequency ω_i of the PSIS. Before the shaking table test, ω_i=0.41 Hz was identified by using a pull-and-released test conducted on the uncontrolled PSIS. The identified for the prototype PSIS is presented in Table 2. Based on the identified ω_i and the rigid-body assumption of the super-structure, the isolation stiffness k_i can be computed by using the frequency equation for an oscillating single DOF

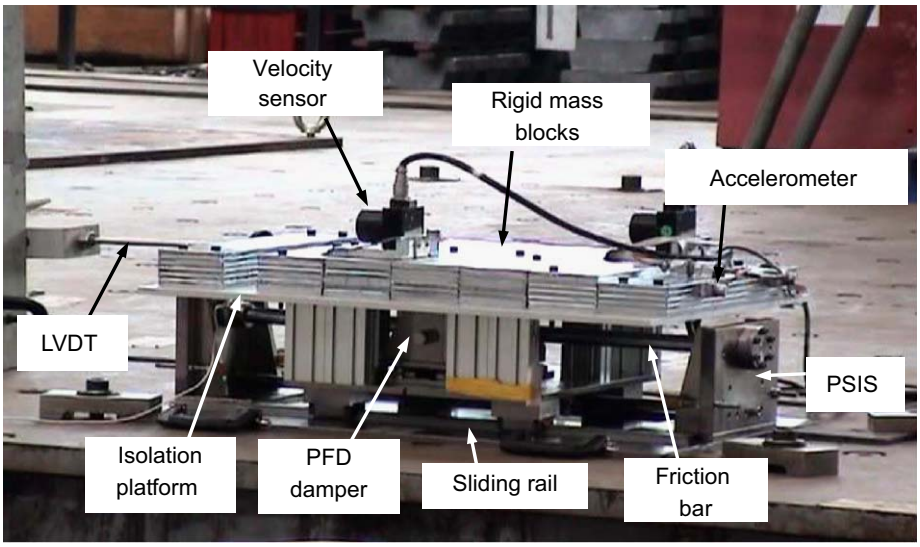

Fig. 9. The prototype PSIS and the test setup.

Table 2
System parameters of the prototype PSIS.

Component	Item	Value
Isolated structure (rigid mass blocks)	Mass (m_s)	75 kg
	Natural frequency (ω_s)	20 Hz
	Damping ratio (ζ_s)	100%
Sliding isolation platform	Mass (m_b)	75 kg
	Isolation stiffness (k_i)	1000 N/m
	Isolation frequency (ω_i)	0.41 Hz
	Friction coefficient of isolator (μ_i)	0.009
	Maximum base displacement (x_b)	$\pm$0.15 m
Piezoelectric friction damper (PFD)	Friction coefficient of damper (μ_d)	0.09
	Damper stiffness (k_d)	10^6 N/m
	Piezoelectric coefficient (C_z)	0.5 N/V
	Pre-compression force (N_0)	60 N
	Range of driving voltage (V)	0–1000 V

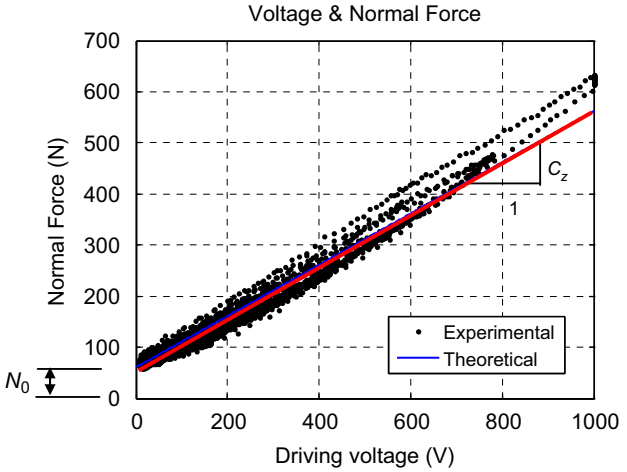

Fig. 10. Experimental relation curve between the force N and voltage V of the PFD.

system: $k_i=\omega_i^2(m_b+m_s)$. As for the estimation of parameters k_s and c_s, both of them were computed from the structural frequency ω_s and damper ratio ζ_s given in Table 2. As presented in the table, in order to simulate the behavior of the rigid superstructure used in the test, a relatively large structural frequency ω_s=20 Hz and damping ratio ζ_s=100% were adopted in this study.

Moreover, Eq. (1) shows that C_z and N_0 are the two most important parameters in controlling the normal force of the PFD. In order to identify these, Fig. 10 plots the experimental relation between the normal force $N(t)$ and the driving voltage $V(t)$, which were measured in a calibration test. Note that a regression line is also depicted in the figure. It is observed in Fig. 10 that $N(t)$ is almost linearly proportional to $V(t)$. Based on Eq. (1), it should be easily realized that the slope of the regression line represents the piezoelectric coefficient C_z, while the intersection of the regression line with the vertical axis of the coordinates (y-axis) signifies the pre-compression force N_0. As listed in Table 1, the values of C_z and N_0 identified from Fig. 10 are 0.5 N/V and 60N, respectively.

5.2. Characteristics of ground motions used in the study

In this study, two acceleration records measured from real earthquakes were used as the input ground excitations. These two ground accelerations, which have very different characteristics, will be used in this section and the experiment section that follows. The detailed information about these two earthquake records is given below: (1) El Centro (S00E) Earthquake, 18 May 1940, peak acceleration 0.341g. (2) Imperial Valley (El Centro Array 6) Earthquake, Channel 1 230°, 15 October 1979, peak acceleration 0.428 g. (3) Chi-Chi (TCU102) earthquake, Channel East-West, 21 September 1999, peak acceleration 0.304 g. The El Centro earthquake is a famous earthquake record that has been widely used in many seismic engineering studies. The Imperial Valley and Chi-Chi earthquake records were recorded from stations near seismic faults, and thus they has very strong near-fault characteristics with a long-period pulse component.

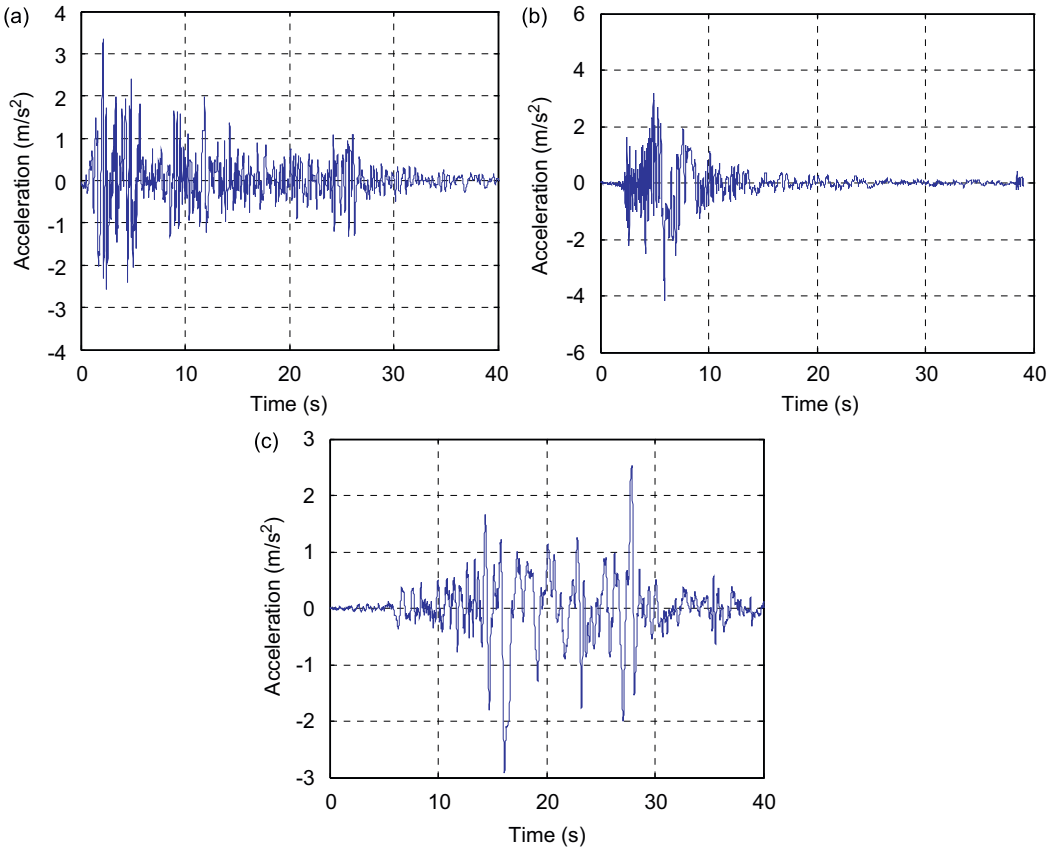

Fig. 11. Waveforms of the three ground accelerations used in this study: (a) El Centro (far field), (b) Imperial Valley (near fault), (c) Chi-Chi (near fault).

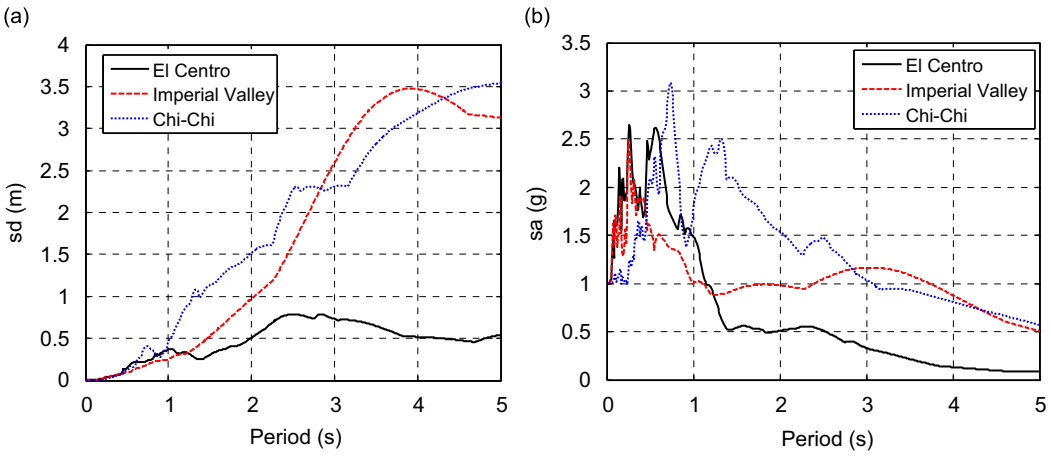

Fig. 12. Normalized displacement and acceleration spectra for the three earthquakes (PGA=1.0 g, 5% damping ratio): (a) displacement spectrum, (b) acceleration spectrum.

The waveforms of the three selected earthquakes are shown in Fig. 11, while Fig. 12 compares their 5%-damping-ratio displacement and acceleration response spectra with their PGA (peak ground acceleration) values normalized to 1.0 g. As shown in Figs. 11(b) and (c), long-period pulse-like waveforms can be clearly observed in the Imperial Valley and Chi-Chi earthquakes. Consequently, Fig. 12 shows that, as compared to the El Centro earthquake, the Imperial Valley and Chi-Chi earthquakes induce larger displacement and acceleration spectral values for a long-period structure whose vibration period is larger than 1.0 s. It is for this reason that in this study the Imperial Valley and Chi-Chi are used to represent typical near-fault earthquakes, whereas the El Centro earthquake represents a typical far-field earthquake.

5.3. Evaluation of control performance for different fuzzy controllers

Fig. 13 compares the simulated peak responses of the three fuzzy controllers listed in Table 1, when the PSIS is subjected to the aforementioned El Centro (far-field), Imperial Valley (near-fault) and Chi-Chi (near-fault) earthquakes. Note that the PGA level of both earthquakes have been scaled to 0.3 g in Fig. 13 for the convenience of cross comparison between the three earthquake responses. In addition, in order to show the control efficiency, the peak responses of an uncontrolled isolation system are also plotted in Fig. 13. The uncontrolled system, whose mathematical model is similar to Fig. 6, except that the PFD damper is removed, may also represent a passive isolation system. This uncontrolled isolation

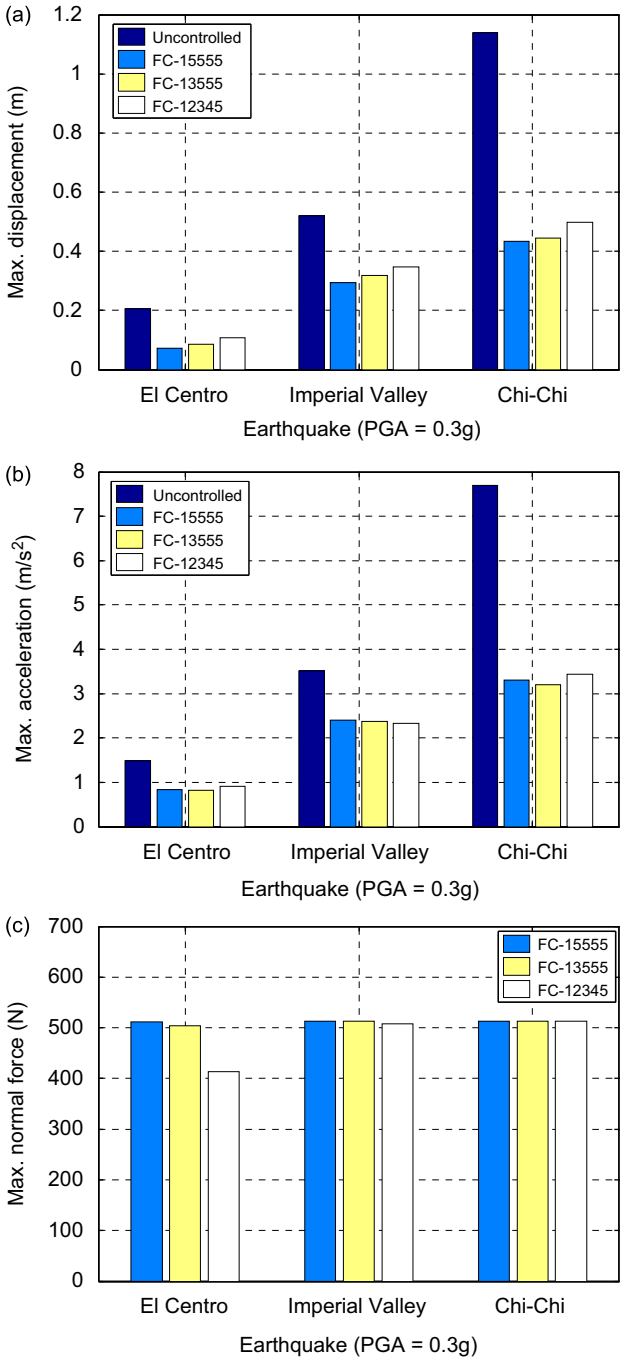

Fig. 13. Comparison of the PSIS peak responses with the three fuzzy controllers: (a) base displacement, (b) structural acceleration, (c) normal force of PFD damper.

system, which has a very low sliding friction coefficient, usually has an excellent isolation performance in regular far-field earthquakes [53]. Moreover, the system parameters listed in Table 2 and the numerical method explained in Section 4 were used in the simulation of all the control cases shown in Fig. 13.

From Fig. 13, it is observed that: (1) as mentioned above, the uncontrolled isolation system has very good performance in the El Centro (far-field) earthquake, since it is able to reduce the transmitted ground acceleration from 0.3 g down to 0.15 g (see Fig. 13(b)). This is equivalent to a 50% reduction in the acceleration response. However, this inevitably induces excessive responses in the Imperial Valley (near-fault) and Chi-Chi (near-fault) earthquakes. The near-fault displacement and acceleration responses of the uncontrolled system have been increased by more than 250% (in Imperial Valley) and 500% (in Chi-Chi) as compared to the far-field responses. (2) As compared to the uncontrolled system, Figs. 13(a) and (b) show that all the proposed fuzzy controllers are very effective in reducing both the base displacement and the transmitted acceleration up to the superstructure. (3) For all types of earthquakes considered, the three controllers have a roughly equal acceleration reduction rate; however, the FC-15555 controller is the best at suppressing the peak base displacement for both types of earthquake (see Fig. 13(a)). Therefore, it may be concluded that the FC-15555 (ABS-type) controller has the best overall isolation performance. (4) To achieve the above control effect, the required maximum clamping force $N(t)$ is about the same for all three fuzzy controllers, except for the FC-12345 controller in the El Centro earthquake (see Fig. 13(c)). Due to the maximum driving voltage that the fuzzy controller can supply (see Fig. 3), the force $N(t)$ actually has an upper bound, which, according to Eq. (1) and Fig. 3, is about 510 N. The reason that the clamping force of the FC-12345 controller does not reach its upper bound in the far-field earthquake could be due to the controller's gentle increase in driving voltage (see Fig. 3) and the PSIS's low sliding velocity in the far-field earthquake.

6. Shaking table test for the prototype PSIS

In order to prove its feasibility and effectiveness, the fuzzy-controlled prototype PSIS described in the previous section was also tested dynamically by using a shaking table test, and the experimental findings from this will be discussed in this section. Since the results in the last section showed that the PSIS with the FC-15555 (ABS-type) controller has the best overall isolation performance, it would be sufficient in this section to only present the test results of this controller. Furthermore, in order to show the connection between the experimental and theoretical studies, all the test data shown in this section will be verified by the numerical simulated results.

6.1. Test setup

Fig. 9 depicts the test setup and the sensor placement for the shaking table test. As shown partially in the figure, velocity sensors and accelerometers were placed on the isolated object (the mass blocks) and also on the shaking table (not shown in the figure). In addition, an LVDT was placed between the isolation platform and a reference frame fixed on the shaking table, in order to measure the relative-to-the-ground base displacement of the prototype PSIS. The clamping force $N(t)$ generated by the piezoelectric actuator was measured by the load cell embedded inside the PFD (see Fig. 2). Notably, since the attached velocity sensors can only measure the absolute velocities physically, in order to obtain the relative velocity of the sliding platform $\dot{x}_b(t)$ for the fuzzy controller, the ground velocity $\dot{x}_g(t)$ must be subtracted from the measured absolute velocity of the mass blocks. $\dot{x}_g(t)$ was measured by another velocity sensor attached on the shaking table.

Moreover, in the test, the acceleration waveforms of the El Centro (far-field) and Imperial Valley (near-fault) earthquakes shown in Figs. 11(a) and (b) were reproduced by the shaking table and used as the input ground motions for the PSIS. For each run, the PGA level of the earthquakes was scaled to an appropriate value, as required. Table 3 lists the PGA levels tested for the two earthquakes in the experiment. The PGA level was increased gradually in order to study the effect of earthquake intensity on the PSIS response. Due to the limitation of the allowable base displacement (± 0.15 m) of the prototype PSIS, the maximum PGA for the El Centro and Imperial Valley earthquakes that could be tested were limited to within 0.35 and 0.25 g, respectively, as presented in Table 3. Note that the Chi-Chi earthquake in Fig. 11 was not considered in the experimental part of this study. The reason is because that the Chi-Chi (near-fault) earthquake has very strong near-fault characteristics with a long-period pulse component, which results in an extremely large ground displacement. Due to the stroke limitation of the shaking table, the Chi-Chi earthquake with sufficient intensity cannot be easily reproduced by the shaking table (earthquake simulator).

Table 3
Ground motions and the PGA values used in the test.

Earthquake name	Property	PGA[a] (g)
El Centro	Far-field earthquake	0.10, 0.20, 0.30, 0.35
Imperial Valley	Near-fault earthquake	0.10, 0.15, 0.20, 0.25

[a] PGA=peak ground acceleration.

6.2. Comparison of experimental and theoretical results

In order to ensure the accuracy of the experiment, in this subsection the test data are verified by the theoretical results simulated by the numerical method given in Section 4. In the simulation, the acceleration signals measured by the accelerometer directly placed on the shaking table are taken as the input ground excitations, and the parametric values listed in Table 2 are used for the PSIS. Figs. 14 and 15 compare the experimental and theoretical responses of the PSIS with the FC-15555 controller, when the system is subjected to the El Centro earthquake (PGA=0.35 g) and the Imperial Valley earthquake (PGA=0.25 g), respectively. Note that each figure contains six sub-figures that represent sequentially: (a) the time-history of the base displacement $x_b(t)$, (b) the time-history of the absolute acceleration of the isolated object $\ddot{x}_{s,a}=(\ddot{x}_s(t)+\ddot{x}_g(t))$, (c) the driving voltage $V(t)$ vs. base velocity $\dot{x}_b(t)$, (d) the time-history of the normal force $N(t)$, (e) the total shear force of the PSIS isolation layer $S_b(t)$ vs. base displacement $x_b(t)$, (f) the PFD damper force $u_d(t)$ vs. base

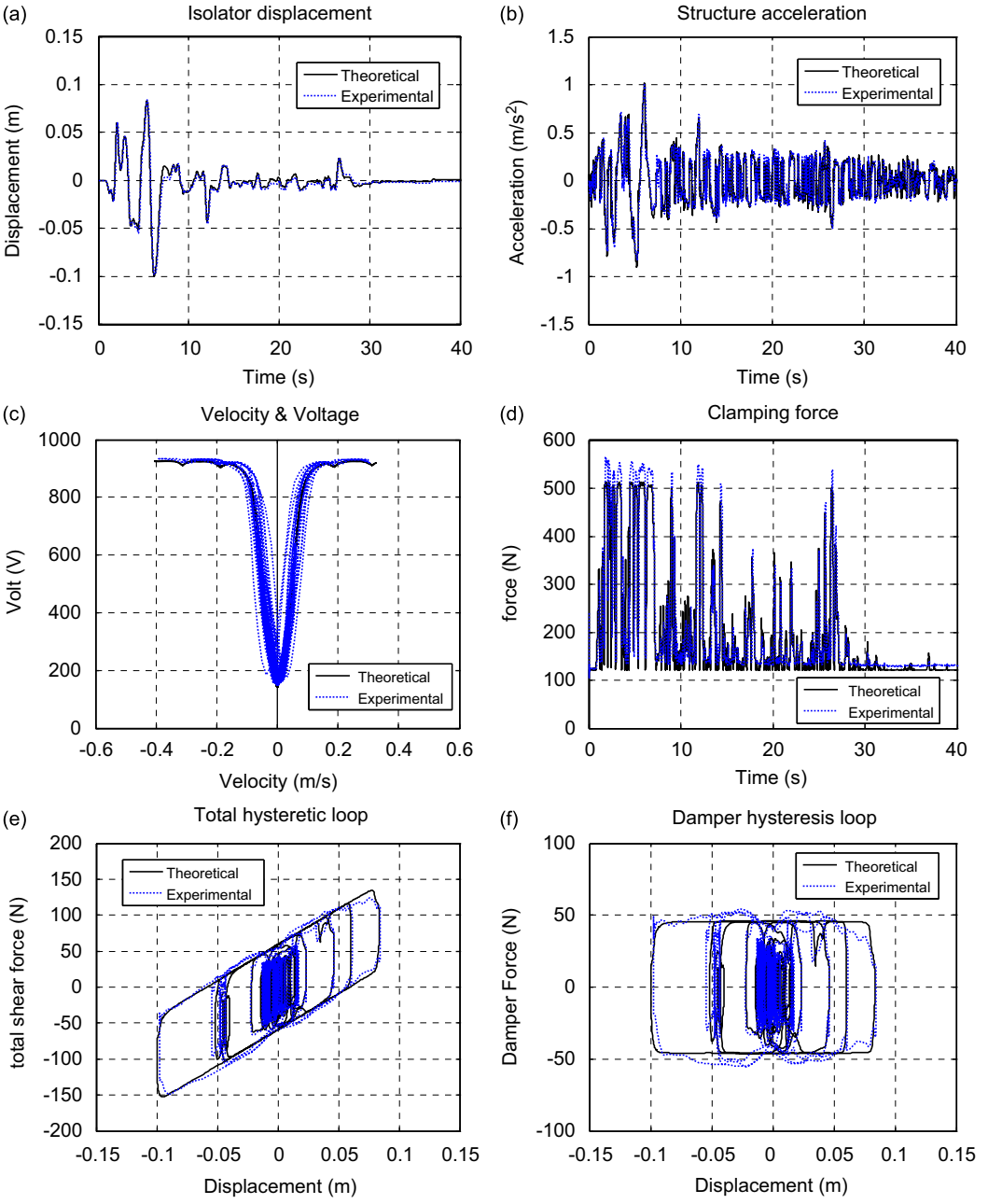

Fig. 14. Comparison of PSIS experimental and theoretical responses for the far-field earthquake (El Centro, PGA=0.35 g): (a) base displacement, (b) structural acceleration, (c) driving voltage vs. base velocity, (d) normal force of PFD, (e) total hysteresis loop of PSIS, (f) hysteresis loop of PFD.

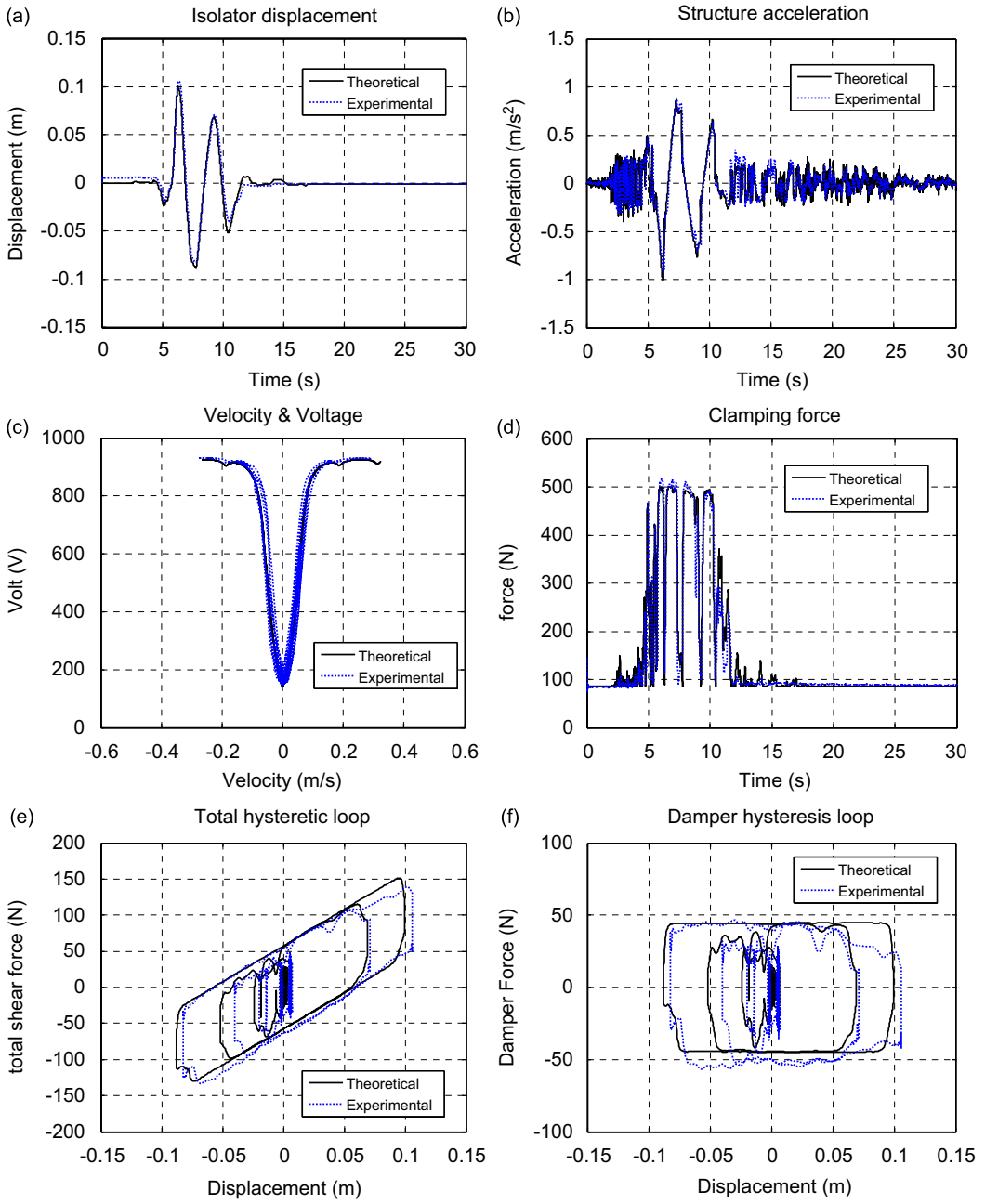

Fig. 15. Comparison of PSIS experimental and theoretical responses for the near-fault earthquake (Imperial Valley, PGA=0.25 g): (a) base displacement, (b) structural acceleration, (c) driving voltage vs. base velocity, (d) normal force of PFD, (e) total hysteresis loop of PSIS, (f) hysteresis loop of PFD.

displacement $x_b(t)$. The sub-figures (e) and (f) of Figs. 14 and 15 are also known as the hysteresis-loops of the PSIS and PFD, respectively, since they clearly demonstrate the hysteretic behaviors of the PSIS and PFD. As shown in Fig. 16, the PSIS total shear $S_b(t)$ is actually the summation of the PFD damper force $u_d(t)$, the platform sliding force $u_i(t)$ and the isolation restoring force $k_i x_b(t)$, i.e.

$$S_b(t) = k_i x_b(t) + u_i(t) + u_d(t) \tag{27}$$

In addition, it should be mentioned that in Figs. 14 and 15 the total shear $S_b(t)$ of the PSIS and the damper force $u_d(t)$ of the PFD shown in the sub-figures (e) and (f) are semi-experimental (indirectly measured) results, which are reconstructed from the test data. The approach of this reconstruction is explained below. Firstly, from Fig. 16 and the dynamic

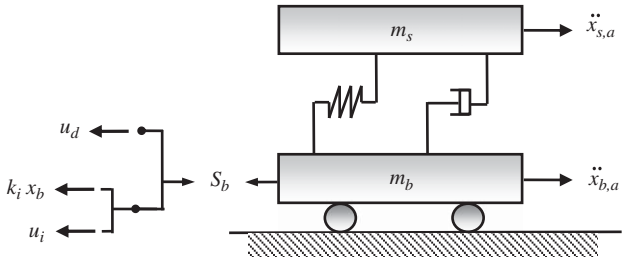

Fig. 16. Total base shear force S_b of the PSIS.

equilibrium condition, the total shear force $S_b(t)$ of the PSIS can also be expressed as

$$S_b(t) = m_s\ddot{x}_{s,a}(t) + m_b\ddot{x}_{b,a}(t) = (m_s + m_b)\ddot{x}_{b,a}(t) \tag{28}$$

where $\ddot{x}_{b,a}(t)$ denotes the absolute acceleration of the PSIS sliding platform. Notably, in above equation, $\ddot{x}_{s,a}(t) = \ddot{x}_{b,a}(t)$ is applied, since the isolated object in the test is a set of rigid blocks. The data of $S_b(t)$ shown in Figs. 14(e) and 15(e) can now be obtained by using Eq. (25), because in the equation m_s and m_b are known prior to the test (see Table 2) and $\ddot{x}_{b,a}(t)$ is measurable by the accelerometer attached to the PSIS platform (see Fig. 9). On the other hand, to obtain the data of $u_d(t)$, firstly let us assume that the PSIS is in its sliding state ($\dot{x}_b(t) \neq 0$), thus the friction force $u_i(t)$ of the sliding platform can be written as

$$u_i(t) = \mathrm{sgn}(\dot{x}_b(t))\mu_i(m_s + m_b)g \tag{29}$$

Next, by using Eqs. (28) and (29) in Eq. (27), one may solve for the force $u_d(t)$ and obtain

$$u_d(t) = (m_s + m_b)\ddot{x}_{b,a}(t) - k_i x_b(t) - \mathrm{sgn}(\dot{x}_b(t))\mu_i(m_s + m_b)g \tag{30}$$

In the last equation, the quantities $\ddot{x}_{b,a}(t)$, $x_b(t)$ and $\dot{x}_b(t)$ are all measurable by the accelerometer, LVDT and velocity sensor attached to the PSIS (see Fig. 9); therefore, the PFD damper force $u_d(t)$ shown in Figs. 14(f) and 15(f) can be obtained by using Eq. (30).

From Figs. 14 and 15, the following observations can be made: (1) generally speaking, regardless of the earthquake type, all the measured data are very consistent with the behavior of the PSIS (FC-15555 controller), as predicted by the numerical analysis, especially for the time history data (see sub-figures (a), (b) and (d)). This means that the test data are reliable, and the PSIS dynamic response can be analyzed by the numerical method. (2) Sub-figures 14(d) and 15(d) clearly demonstrate that the normal force $N(t)$ of the PFD damper can be altered by the embedded piezoelectric actuator. This behavior cannot be achieved with a passive friction damper, which usually has a constant normal force. (3) The voltage–velocity relation curves shown in Figs. 14(c) and 15(c) are very similar to the theoretical curve of the FC-15555 controller shown in Fig. 5. (4) Due to the complicated friction behavior, as well as measurement noise, the experimental and theoretical hysteresis loops of the PFD have a relatively larger discrepancy (see Figs. 14(f) and 15(f)), as compared to the other system responses. Nevertheless, this discrepancy does not significantly affect the global responses of the PSIS, because both the experimental displacement and acceleration responses match very well with the theoretical results in sub-figures (a) and (b) of Figs. 14 and 15.

6.3. Experimental evaluation of the isolation efficiency of the PSIS (FC-15555)

In order to investigate the isolation efficiency of the PSIS with the FC-15555 controller, in this subsection the experimental seismic responses of the PSIS are compared with the simulated responses of its uncontrolled counterpart system, which is mentioned in Section 5.3 and Fig. 13. The reason for using the simulated responses for the uncontrolled system, instead of the experimental ones, is because the base displacement of the uncontrolled system can easily exceed the allowable displacement of the prototype PSIS, which is 0.15 m, even in a small earthquake. This would make the comparison for earthquakes with larger PGA levels become impossible. Moreover, in order to facilitate a fair comparison, in the simulation of the uncontrolled system, the same ground acceleration as measured in the PSIS shaking table test and the same system parametric values as presented in Table 1 will be used.

(1) *Evaluation by time-history responses*: Figs. 17 and 18 compare the time-history responses of the PSIS (FC-15555) and the uncontrolled system, when they are subjected to the far-field earthquake (El Centro, PGA=0.35 g) and the near-fault earthquake (Imperial Valley, PGA=0.25 g), respectively. From Figs. 17 and 18, it is evident that in both the near-fault and the far-field earthquakes, the proposed PSIS is very effective in reducing the structural acceleration and the isolator displacement simultaneously, as compared to the uncontrolled isolation system. This simultaneous reduction is usually very difficult to achieve with a passive isolation system. Moreover, in the near-fault earthquake (see Fig. 18), both the acceleration and displacement responses of the uncontrolled system exhibit a long-period oscillation, whereas the PSIS very effectively suppresses the oscillation in a very short period of time. This implies that the PSIS is especially suitable for near-fault earthquakes.

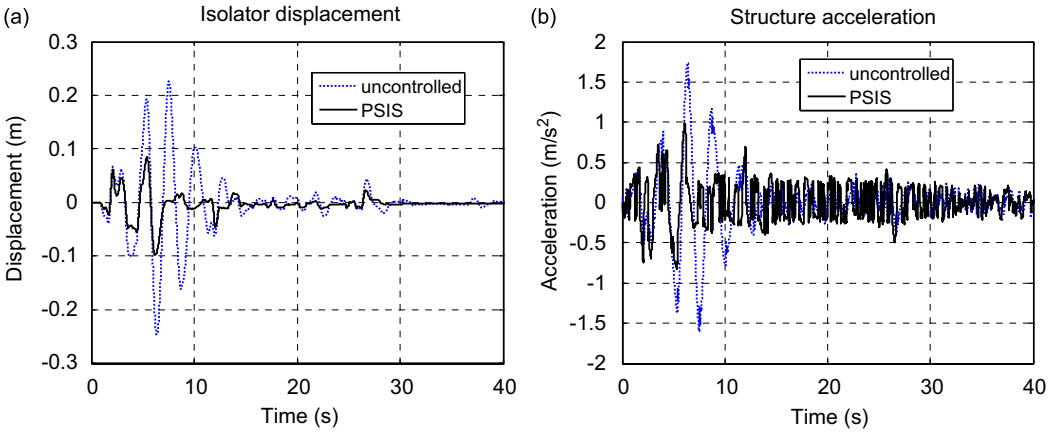

Fig. 17. Comparison of the PSIS and uncontrolled responses for the far-field earthquake (El Centro, PGA=0.35 g): (a) base displacement, (b) structural acceleration.

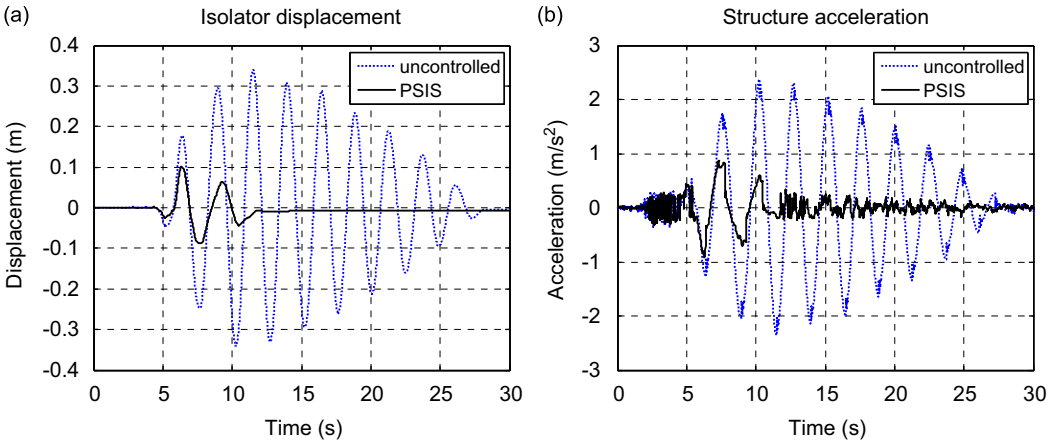

Fig. 18. Comparison of the PSIS and uncontrolled responses for the near-fault earthquake (Imperial Valley, PGA=0.25 g): (a) base displacement, (b) structural acceleration.

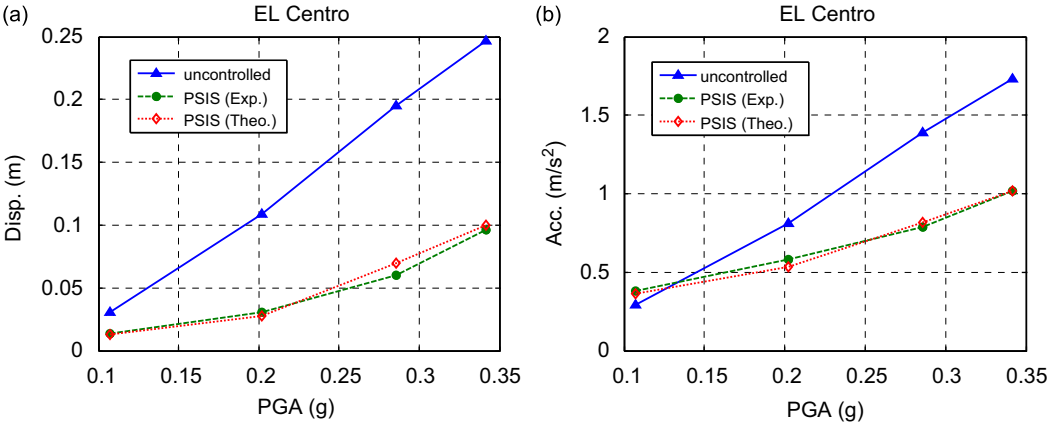

Fig. 19. Comparison of PSIS and uncontrolled peak responses for the far-field (El Centro) earthquake with different PGA levels: (a) peak base displacement, (b) peak structural acceleration.

(2) *Evaluation of peak responses for different PGA levels*: Because earthquake intensity is usually unpredictable, it would be beneficial to investigate how the PSIS (FC-15555) performs in earthquakes with different intensities. Figs. 19 and 20 compare the peak responses of the PSIS and the uncontrolled systems, when they are subjected to the two earthquakes

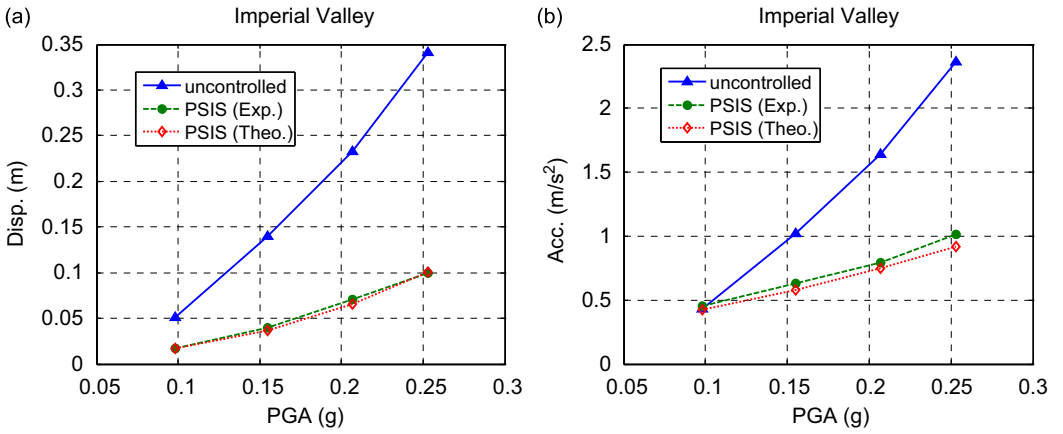

Fig. 20. Comparison of PSIS and uncontrolled peak responses for the near-fault (Imperial Valley) earthquake with different PGA levels: (a) peak base displacement, (b) peak structural acceleration.

Table 4
Definition of performance indices.

Response	Peak base displacement	RMS base displacement
Index[a]	$J_1=\frac{\max(x_b(t))}{\max(\overline{x}_b(t))}$	$J_2=\frac{RMS(x_b(t))}{RMS(\overline{x}_b(t))}$
Response Index[a]	Peak structural acceleration $J_3=\frac{\max(\ddot{x}_{s,a}(t))}{\max(\overline{\ddot{x}}_{s,a}(t))}$	RMS structural acceleration $J_4=\frac{RMS(\ddot{x}_{s,a}(t))}{RMS(\overline{\ddot{x}}_{s,a}(t))}$
Force Index	Peak friction force of PFD damper $J_5=\frac{\max(u_d(t))}{W}$	

[a] A symbol with a top-bar represents the response of the uncontrolled system.

with the various PGA levels listed in Table 3. Note that in the figures both the experimental and theoretical data are plotted for the PSIS. From Figs. 19 and 20, it is clearly observed that: (1) the accuracy of the test results for all tested PGA levels are confirmed by the high consistency between the experimental and theoretical data. (2) In both the near-fault and far-field earthquakes, the displacement and acceleration performance of the PSIS are superior to those of the uncontrolled case in a PGA level larger than 0.15 g. A larger PGA leads to a higher response reduction rate for the PSIS. (3) For the acceleration response, the uncontrolled system may outperform the PSIS only in a far-field earthquake with a PGA <0.15 g (see Fig. 19(b)). However, in this level of PGA, the earthquake has only a minor effect on the isolated system. (4) The uncontrolled passive isolation system encounters excessive acceleration and displacement responses in the near-fault earthquake. The PSIS is especially effective in suppressing these excessive peak responses.

(3) *Evaluation by performance indices*: In order to quantify the results of the comparison, five performance indices (J_1–J_5) defined in Table 4 are employed to evaluate the performances of the PSIS (FC-15555) in this subsection. The indices J_1 and J_3 in Table 4 represent the peak response ratios of the base (isolation platform) displacement $x_b(t)$ and structural (isolated object) acceleration $\ddot{x}_{s,a}(t)$ of the PSIS, respectively. The indices J_2 and J_4 represent the RMS response ratios of $x_b(t)$ and $\ddot{x}_{s,a}(t)$, respectively. Note that the indices J_1–J_4 have all been divided by the corresponding response values of the uncontrolled isolation system, which are represented by the symbols with a top bar in Table 4. Therefore, for indices J_1–J_4, a value less than one implies that the PSIS has a lower response than that of the uncontrolled system. As for the performance index J_5, it represents the ratio of the peak PFD damper force (slip force) to the total weight W of the system.

Table 5 presents the values of the performance indices for the PSIS (FC-15555) subjected to the two earthquakes with various PGA levels. The average of each index is also given in the table. The following observations can be made from Table 5: (1) for the far-field earthquake with a PGA >0.2 g and the near-fault earthquake with a PGA larger than 0.15 g, the PSIS is able to simultaneously suppress the displacement and acceleration response of the system, since all the indices are less than one. Overall, the larger the PGA is, the greater the reduction rate that the PSIS will obtain. For the earthquakes with the largest PGA (0.25 and 0.35 g), the peak displacement and acceleration indices J_1 and J_3 can be down to 0.30–0.34 and 0.39–0.58, respectively. (2) In the far-field and the near-fault earthquakes, the PSIS is able to suppress the peak base displacement (see index J_1) down to an average of 34% and 28% of the uncontrolled system, respectively; meanwhile, it also reduces the peak acceleration (see index J_3) down to an average of 79% and 62% of the uncontrolled system in the far-field and near-fault earthquakes, respectively. (3) The PSIS is much more effective in mitigating the seismic response due to the

Table 5
Performance indices for the PSIS (FC-15555).

Earthquake	PGA (g)	Displacement index		Acceleration index		Force index
		J_1 (Peak)	J_2 (RMS)	J_3 (Peak)	J_4 (RMS)	J_5
El Centro (far-field)	0.10	0.322	0.733	1.301	1.284	0.025
	0.20	0.303	0.439	0.738	1.059	0.032
	0.30	0.325	0.332	0.555	0.783	0.035
	0.35	0.397	0.349	0.576	0.656	0.038
	Average	0.337	0.463	0.793	0.946	0.033
Imperial Valley (Near-fault)	0.10	0.300	0.206	1.046	0.770	0.029
	0.15	0.268	0.162	0.606	0.380	0.032
	0.20	0.265	0.180	0.455	0.271	0.037
	0.25	0.298	0.164	0.389	0.232	0.039
	Average	0.283	0.178	0.624	0.413	0.034

near-fault earthquake than the far-field one. It is also shown that the PSIS is more effective in suppressing the base displacement (J_1 and J_2) than the structural acceleration (J_3 and J_4) in terms of either the peak or RMS value. (4) For the far-field (El Centro) earthquake with a very low intensity (PGA=0.1 g), the PSIS still has a lower base displacement, although it may induce a slightly larger acceleration response than those of the uncontrolled system (see J_3 and J_4). However, it must be emphasized again that the uncontrolled system actually represents a very efficient passive isolation system for regular far-field earthquakes. Thus, the acceleration response of the PSIS is actually very low in the far-field earthquake when PGA=0.1 g, and would have an insignificant effect on the isolated object. (5) Finally, from index J_5, the required PFD peak slip forces have an average of about 3.4% of the total system weight; however, it should be remembered that this force is a passive resistant force provided by the friction interface in the PFD. Due to the voltage limitation, the allowable peak slip force of the PFD is about 50 N, which is about 3.4% of the total weight.

7. Conclusions

In order to improve the performance of seismic isolation systems subjected to near-fault earthquakes, a semi-active isolation system, called a Piezoelectric Seismic Isolation System (PSIS), that is controlled by a simple fuzzy controller, is investigated theoretically and experimentally in this study. The PSIS is mainly composed of a sliding isolation platform and a piezoelectric friction damper (PFD). The dynamic response of the PSIS is attenuated by regulating the slip force of the PFD, which is driven by an embedded piezoelectric actuator. The fuzzy rule of the fuzzy controller is designed according to the control logic of antilock braking systems (ABS). In order to prevent an excessive base displacement, the adopted ABS-type fuzzy controller will rapidly increase the PFD damper force to a maximal value, whenever the sliding velocity of the PSIS starts to increase. On the other hand, whenever the PSIS is going to cease its sliding motion, the controller will swiftly reduce the PFD damper force to a minimal value, so that the PSIS will maintain it isolation function and the ground acceleration transmitted onto the isolated object can be minimized. The proposed fuzzy controller is very easily implemented, since it only requires the measurement of the PSIS's sliding velocity.

In order to demonstrate the isolation effectiveness of the fuzzy-controlled PSIS, both theoretical and experimental studies were conducted for a prototype PSIS in this paper. The theoretical result, which was analyzed by the proposed numerical method, shows that the proposed ABS-type fuzzy controller has better performance than the other types of fuzzy controllers. A dynamic test using a shaking table (seismic simulator) was then conducted on the prototype PSIS for the experimental verification. The test results show that the measured data have very good agreement with the simulated theoretical results. This confirms the accuracy of the test data, and also the feasibility of the PSIS. The experimental results also demonstrate that for either the far-field or the near-fault earthquakes, the PFD damper with the proposed ABS-type fuzzy controller is able to simultaneously suppress the base displacement and reduce the transmitted acceleration response of the PSIS subjected to an earthquake with a peak ground acceleration greater than about 0.15 g. It is also shown by the test data that the fuzzy controlled PSIS is especially effective in near-fault earthquakes, in which the peak base displacement and the transmitted acceleration can be reduced down to an average value of about 30% and 60%, respectively, as compared to the responses of the uncontrolled isolation system.

Acknowledgments

This research was sponsored in part by the National Science Council of R.O.C. (Taiwan), through Grant 96-2221-E-327-019. This support is gratefully acknowledged. The authors are also grateful to the National Center for Research on Earthquake Engineering (NCREE, Taiwan) for their technical support on the shaking table test.

References

[1] L.Y. Lu, Y.B. Yang, Dynamic response of equipment in structures with sliding support, *Earthquake Engineering and Structural Dynamics* 26 (1997) 61–76.
[2] F. Naeim, J.M. Kelly, *Design of Seismic Isolated Structures*, Wiley, New York, 1999 (Chapter 4).
[3] Y.B. Yang, L.Y. Lu, J.D. Yau, in: C.W. de Silva (Ed.), *Vibration and Shock Handbook*, CRC Press, Taylor & Francis Group, Boca Raton, Florida, 2005 (Chapter 22).
[4] R.S. Jangid, J.M. Kelly, Base isolation for near-fault motion, *Earthquake Engineering and Structural Dynamics* 30 (2001) 691–707.
[5] J.F. Hall, Seismic response of steel frame buildings to near-source ground motions, *Earthquake Engineering and Structural Dynamics* 27 (1998) 1445–1464.
[6] J.W. Baker, Quantitative classification of near-fault ground motions using wavelet analysis, *Bulletin of the Seismological Society of America* 97 (2007) 1486–1501.
[7] L.Y. Lu, M.H. Shih, C.S. Chang Chien, W.N. Chang, Seismic performance of sliding isolated structures in near-fault areas, *Proceedings of the 7th US National Conference on Earthquake Engineering*, Session AT-2, July 21–25, 2002, Boston, MA, USA.
[8] S. Narasimhan, S. Nagarajaiah, H. Gavin, E.A. Johnson, Smart base isolated benchmark building part I: problem definition, *Structural Control and Health Monitoring* 13 (2006) 573–588.
[9] Y. Liu, T.P. Waters, M.J. Brennan, A comparison of semi-active damping control strategies for vibration isolation of harmonic disturbances, *Journal of Sound and Vibration* 280 (2005) 21–39.
[10] H.P. Gavin, A. Zaicenco, Performance and reliability of semi-active equipment isolation, *Journal of Sound and Vibration* 306 (2007) 74–90.
[11] T.Y. Lee, K. Kawashima, Semi-active control of nonlinear isolated bridges with time delay, *Journal of Structural Engineering (ASCE)* 133 (2007) 235–241.
[12] S.J. Dyke, B.F. Spencer Jr., M.K. Sain, J.D. Carlson, Modeling and control of magnetorheological dampers for seismic response reduction, *Smart Materials and Structures* 5 (1996) 565–575.
[13] S.J. Dyke, B.F. Spencer Jr., M.K. Sain, J.D. Carlson, Experimental study of MR dampers for seismic protection, *Smart Materials and Structures* 7 (1998) 693–703.
[14] G. Yan, L.L. Zhou, Integrated fuzzy logic and genetic algorithms for multi-objective control of structures using MR dampers, *Journal of Sound and Vibration* 296 (2006) 368–382.
[15] D.A. Shook, P.N. Roschke, P.Y. Lin, C.H. Loh, GA-optimized fuzzy logic control of a large-scale building for seismic loads, *Engineering Structures* 30 (2008) 436–449.
[16] U. Aldemir, Causal semi-active control of seismic response, *Journal of Sound and Vibration* 322 (2009) 665–673.
[17] J.N. Yang, J. Bobrow, F. Jabbari, J. Leavitt, C.P. Cheng, P.Y. Lin, Full-scale experimental verification of resetable semi-active stiffness dampers, *Earthquake Engineering and Structural Dynamics* 36 (2007) 1255–1273.
[18] L.Y. Lu, G.L. Lin, Improvement of near-fault seismic isolation using a resetable variable stiffness damper, *Engineering Structures* 31 (2009) 2097–2114.
[19] S. Nagarajaiah, S. Sahasrabudhe, Seismic response control of smart sliding isolated buildings using variable stiffness systems: an experimental and numerical study, *Earthquake Engineering and Structural Dynamics* 35 (2006) 177–197.
[20] L.Y. Lu, G.L. Lin, T.C. Kuo, Stiffness controllable isolation system for near-fault seismic isolation, *Engineering Structures* 30 (2008) 747–765.
[21] Y. Liu, H. Matsuhisa, H. Utsuno, Semi-active vibration isolation system with variable stiffness and damping control, *Journal of Sound and Vibration* 313 (2008) 16–28.
[22] C. Chen, G. Chen, Shaking table test of quarter-scale building model with piezoelectric friction dampers, *Structural Control and Health Monitoring* 11 (2004) 239–257.
[23] L.Y. Lu, G.L. Lin, A theoretical study on piezoelectric smart isolation system for seismic protection of equipment in near-fault areas, *Journal of Intelligent Material Systems and Structures* 20 (2009) 217–232.
[24] B.F. Spencer, S. Nagarajaiah, State of the art of structural control, *Journal of Structural Engineering* 129 (2003) 845–856.
[25] P.B. Muanke, P. Masson, P. Micheau, Determination of normal force for optimal energy dissipation of harmonic disturbance in a semi-active device, *Journal of Sound and Vibration* 311 (2008) 633–651.
[26] S. Kannan, H.M. Uras, H.M. Aktan, Active control of building seismic response by energy dissipation, *Earthquake Engineering and Structural Dynamics* 24 (1995) 747–759.
[27] D.J. Dowdell, S. Cherry, On passive and semi-active friction damping for seismic response control of structures, *Proceedings of the 11th World Conference on Earthquake Engineering*, Acapulco, Mexico, Elsevier Science, Oxford, Disc 2, 1996, Paper 957.
[28] J.A. Inaudi, Modulated homogeneous friction: a semi-active damping strategy, *Earthquake Engineering and Structural Dynamics* 26 (1997) 361–376.
[29] C.L. Ng, Y.L. Xu, Semi-active control of a building complex with variable friction dampers, *Engineering Structures* 29 (2007) 1209–1225.
[30] L.Y. Lu, Predictive control of seismic structures with semi-active friction dampers, *Earthquake Engineering and Structural Dynamics* 33 (2004) 647–668.
[31] L.Y. Lu, L.L. Chung, G.L. Lin, A general method for semi-active feedback control of variable friction dampers, *Journal of Intelligent Material Systems and Structures* 15 (2004) 393–412.
[32] L.Y. Lu, G.L. Lin, Predictive control of smart isolation system for precision equipment subjected to near-fault earthquakes, *Engineering Structures* 30 (2008) 3045–3064.
[33] L.A. Zadeh, Fuzzy sets, *Information and Control* 8 (1965) 338–353.
[34] E.H. Mamdani, Application of fuzzy algorithms for control of simple dynamic plants, *Proceeding of the IEE*, 1974, pp. 1585–1588.
[35] K.M. Choi, S.W. Cho, H.J. Jung, I.W. Lee, Semi active fuzzy control for seismic response reduction using magnetorheological dampers, *Earthquake Engineering and Structural Dynamics* 33 (2004) 723–736.
[36] T. Sun, Z. Huang, D. Chen, Signal frequency-based semi-active fuzzy control for two-stage vibration isolation system, *Journal of Sound and Vibration* 280 (2005) 965–981.
[37] A.P. Wang, Y.H. Lin, Vibration control of a tall building subjected to earthquake excitation, *Journal of Sound and Vibration* 299 (2007) 757–773.
[38] R. Guclu, H. Yazici, Vibration control of a structure with ATMD against earthquake using fuzzy logic controllers, *Journal of Sound and Vibration* 318 (2008) 36–49.
[39] M.K. Bhardwaj, T.K. Datta, Semi-active fuzzy control of the seismic response of building frames, *Journal of Structural Engineering (ASCE)* 132 (2006) 791–799.
[40] L.Y. Lu, G.L. Lin, Fuzzy logic control for seismic structures with semi-active friction dampers, *Journal of the Chinese Institute of Civil and Hydraulic Engineering* 20 (2008) 81–95.
[41] A.S. Ahlawat, A. Ramaswamy, Multi-objective optimal fuzzy logic controller driven active and hybrid control systems for seismically excited nonlinear buildings, *Journal of Engineering Mechanics (ASCE)* 130 (2004) 416–423.
[42] D.G. Reigles, M.D. Symans, Supervisory fuzzy control of a base-isolated benchmark building utilizing a neuro-fuzzy model of controllable fluid viscous dampers, *Structural Control and Health Monitoring* 13 (2006) 724–747.
[43] G. Song., H. Sethib, H.N. Li, Vibration control of civil structures using piezoceramic smart materials: a review, *Engineering Structures* 28 (2006) 1513–1524.

[44] P.Y. Lin, P.N. Roschke, C.H. Loh, Hybrid base-isolation with magneto-rheological damper and fuzzy control, *Structural Control and Health Monitoring* 14 (2007) 384–405.
[45] J.W. Douglas, T.C. Schafer, The Chrysler sure brake: the first production four-wheel anti-skid system, SAE Technical Paper 710248, 1971.
[46] G.F. Mauer, A fuzzy logic controller for an ABS braking system, *IEEE Transactions on Fuzzy Systems* 3 (1995) 381–388.
[47] A. Mirzaei, M. Moallem, B.M. Dehkordi, B. Fahimi, Design of an optimal fuzzy controller for antilock braking systems, *IEEE Transactions on Vehicular Technology* 55 (2006) 1725–1730.
[48] A.E. Schwaller, *Motor Automotive Technology*, third ed., Delmar Publishers an International Thomson Publishing Company, 1999, pp. 825–827.
[49] N. Derek, B. Allen, *A Practical, Approach to Motor Vehicle Engineering and Maintenance*, second ed., Elsevier Butterworth Heinemann, 2005, pp. 195–196.
[50] L. Meirovitch, *Concept from Linear System Theory. Dynamics and Control of Structures*, Wiley, New York, 1990 (Chapter 3).
[51] Y.P. Wang, W.H. Liao, C.L. Lee, A state-space approach for dynamic analysis of sliding structures, *Engineering Structures* 23 (2001) 790–801.
[52] L.Y. Lu, L.L. Chung, L.Y. Wu, G.L. Lin, Dynamic analysis of structures with friction devices using discrete-time state-space formulation, *Computers and Structures* 84 (2006) 1049–1071.
[53] R.S. Jangid, Optimum frictional elements in sliding isolation systems, *Computers and Structures* 76 (2000) 651–661.